Influence of Nuclear Structure on Decay Properties of Heavy Nuclei

Ward, Daniel

2017

Document Version:
Publisher's PDF, also known as Version of record

Influence of Nuclear Structure on Decay Properties of Heavy Nuclei

by Daniel E. Ward

LUND
UNIVERSITY

Dissertation for the degree of
Doctor of Philosophy in Engineering
Thesis advisors: Sven Åberg, B. Gillis Carlsson
Faculty opponent: Stefan Frauendorf

Academic dissertation which, by due permission of the Faculty of Engineering at Lund University, will be publicly defended on Friday, January 13th, 2017, at 13:15 in the Rydberg lecture hall (Rydbergsalen) at the Department of Physics, Sölvegatan 14A, Lund, for the degree of Doctor of Philosophy in Engineering.

Organization
LUND UNIVERSITY

Department of Physics
Division of Mathematical Physics
Box 118, 221 00 LUND,
Sweden

Author(s)
Daniel E. Ward

Document name
DOCTORAL DISSERTATION

Date of issue
2017-01-13

Sponsoring organization

Title
Influence of Nuclear Structure on Decay Properties of Heavy Nuclei

Abstract
This dissertation deals with the effects of nuclear structure on the α-decay properties, and on the fission-yield distributions from the decay of heavy nuclei. The nuclear-structure and decay properties of superheavy nuclei is one of the central topics for investigation. α decay is treated in a microscopic approach employing Skyrme-Hartree-Fock-Bogoliubov wave functions to describe the formation of an α cluster in the unstable nucleus. Fission is treated using the random-walk approach, where the nuclear level density obtained from a detailed model influences the dynamical evolution of the shape of the nucleus. The dissertation contains five original research papers, and an introductory part containing background information and some additional details of the studies.

Paper I contains an investigation of the α-particle formation amplitudes and decay rates obtained with Skyrme-Hartree-Fock-Bogoliubov wave functions for even-even near-spherical nuclei.

Paper II contains a study of some more aspects of the description in Paper I.

Paper III extends the application of the method in papers I and II to odd-mass near-spherical nuclei. Hindrance factors and the competition between α-decay paths to different excited states are investigated.

Paper IV deals with the theoretical description of low-lying states in superheavy nuclei observed in α-decay and spectroscopy measurements on element 115 decay chains.

Paper V contains results for fission-yield distributions obtained by combining the nuclear level densities from a combinatorial model with the five-dimensional shape space random-walk approach. The influence on the yields from the structure of the microscopically calculated level densities is investigated.

Key words
alpha decay, hindrance factors, Skyrme-Hartree-Fock-Bogoliubov model, superheavy nuclei, fission yields, Brownian-shape motion, nuclear structure, nuclear level density

Classification system and/or index terms (if any)

Supplementary bibliographical information

Language
English

ISSN and key title

ISBN
978-91-7753-120-3 (print)
978-91-7753-121-0 (pdf)

Recipient's notes

Number of pages
76

Price

Security classification

Influence of Nuclear Structure on Decay Properties of Heavy Nuclei

by Daniel E. Ward

LUND
UNIVERSITY

A doctoral thesis at a university in Sweden takes either the form of a single, cohesive research study (monograph) or a summary of research papers (compilation thesis), which the doctoral student has written alone or together with one or several other author(s).

In the latter case the thesis consists of two parts. An introductory text puts the research work into context and summarizes the main points of the papers. Then, the research publications themselves are reproduced, together with a description of the individual contributions of the authors. The research papers may either have been already published or are manuscripts at various stages (in press, submitted, or in draft).

Faculty of Engineering, LTH, Department of Physics
Division of Mathematical Physics

ISBN: 978-91-7753-120-3 (print)
ISBN: 978-91-7753-121-0 (pdf)

Printed in Sweden by Media-Tryck, Lund University, Lund 2016

Acknowledgments

First, I would like to thank my two thesis advisors, Sven Åberg and Gillis Carlsson, for introducing me to the exciting field of theoretical nuclear-structure and nuclear many-body physics, and giving me the opportunity to do research with them. Next, I want to thank Dirk Rudolph for suggesting research topics and interesting discussions connected to superheavy nuclei. I am grateful to Peter Möller for his hospitality during my visit to Los Alamos National Lab, and for the fruitful collaboration. I would also like to thank Ingemar Ragnarsson, Thomas Døssing, and Jørgen Randrup for the collaboration, as well as for sharing their knowledge and experience in nuclear physics. Lastly, I would like to thank the staff at the division of Mathematical Physics for the great working atmosphere. My PhD studies would not have been as enjoyable without the great social atmosphere among the students at the division. Thanks also to all of the senior researchers who took the time to set up and give advanced courses for the PhD students.

Populärvetenskaplig sammanfattning

Atomkärnan står för den stora merparten av massan i en atom och kan beskrivas som en samling protoner och neutroner (kärnpartiklar). Många olika kombinationer av antal protoner Z och antal neutroner N kan sättas samman och bilda en atomkärna, men de flesta atomkärnor är inte stabila utan sönderfaller efter en tid. Det radioaktiva sönderfallet innebär att byggstenarna i atomkärnan spontant ändrar om sig till en mer gynnsam konfiguration.

I denna avhandling undersöks sönderfall av tunga atomkärnor med hjälp av detaljerade teoretiska modeller. Metoder för att beskriva α-sönderfall och fission utvecklas genom att kombinera moderna modeller för atomkärnans form och struktur med modeller för de dynamiska processer som ger upphov till sönderfall. α-sönderfall innebär att en atomkärna delar upp sig i en Heliumkärna (α-partikel) och en ny dotterkärna med två färre protoner och två färre neutroner. Vi visar att den väletablerade Skyrme-Hartree-Fock-Bogoliubov strukturmodellen, som ger en bra beskrivning av bland annat kärnans bindningsenergi och form, även ger en bra beskrivning av relativa sönderfallssannolikheter i olika tävlande α-sönderfallsvägar. De olika sönderfallsvägarna utgörs av att dotterkärnan hamnar i olika exciterade tillstånd. Med den utvecklade metoden kan strukturens betydelse för vilken väg som tas studeras i många olika kärnor. Metoden tillämpas för att förutsäga när dotterkärnan hamnar i ett exciterat tillstånd efter utsändning av en α-partikel från s.k. supertunga atomkärnor (se nedan). När detta sker kan sedan den exciterade kärnan sända ut röntgenstrålning, och genom att mäta denna och liknande strålning i experiment kan man identifiera grundämnet och få viktig information om strukturen i kärnan.

Fission innebär en uppdelning av en atomkärna i två ungefär lika stora kärnor. Fission av tunga kärnor kan induceras genom beskjutning med en neutron. Med en ny metod gör vi förutsägelser för fissionsuppdelningens beroende av neutronenergin. Vi beräknar hur strukturen i atomkärnan ger upphov till ett komplicerat energiberoende för hur sannolikt det är att båda fragmenten från fissionen blir lika stora. I beräkningarna tydliggörs även att kärnpartiklarnas tendens att para ihop sig två-och-två spelar en viktig roll under fissionsprocessen.

Inget av de kända grundämnena tyngre än Vismut är stabila, utan samtliga sönderfaller

till lättare grundämnen. I naturen skapas tunga grundämnen i våldsamma astrofysikaliska processer i universum. I vissa fall som t.ex. Uran kan de vara långlivade nog för att hittas i solsystem miljarder år senare. Hur tunga atomkärnor som kan existera, och därmed var det periodiska systemet tar slut, är en fråga som aktivt undersöks inom kärnfysikens grundforskning[1]. Den kvantmekaniska skalstrukturen för protoner och neutroner, likande skalen för elektronerna i atomen som ger upphov till ädelgaser vid fyllda skal, möjliggör existensen av supertunga ($Z \geq 104$) grundämnen. Teoretiska modeller förutsäger att slutna skal kan ge upphov till mycket långlivade supertunga grundämnen. Det förutspådda läget i N-Z-planet för dessa skal ligger bortom hittills kända grundämnen, och kan liknas med en ö i ett outforskat hav. Eftersom modellerna är anpassade för att beskriva kända atomkärnor, så kan tillämpningen i okända områden innebära stora fel i förutsägelserna.

I experiment har man lyckats skapa supertunga kärnor upp till $Z = 118$, som nyligen fick namnet Oganesson efter Yuri Oganessian, chefen för forskargruppen på laboratoriet i Dubna, Ryssland, där upptäckten gjordes. Hittills är det dock en bit kvar till möjliga lägen för den stabila ön, framförallt i antal neutroner. För att förbättra modellerna är det viktigt att ha så mycket säker information som möjligt om strukturen hos de ämnen som går att skapa experimentellt. Med hjälp av detta kan man falsifiera teoretiska förutsägelser och få en bättre inblick i de fenomen, exempelvis ökande påverkan av många positivt laddade protoner i kärnan, som blir viktigare i de supertunga kärnorna än i de mer välstuderade grundämnena. Utvecklingen av en detaljerad teoretisk beskrivning av α-sönderfall som görs i den här avhandlingen kan förhoppningsvis bidra som ett led i detta arbete, med målet att kartlägga den yttre gränsen för det periodiska systemet.

Fission är den grundläggande processen som utnyttjas för att generera energi i dagens kärnkraftsreaktorer. Sett ur ett teoretiskt perspektiv är fissionsprocessen mycket utmanande att beskriva, då det handlar om ett stort antal starkt växelverkande kärnpartiklar som rör sig tillsammans under uppdelningen. I den här avhandlingen undersöks hur strukturen hos de exciterade tillstånden i systemet kan påverka processen. Resultaten kan direkt användas för att göra förutsägelser om fördelningen av fissionsfragmentens massa, och undersökningen kan förhoppningsvis öka förståelsen för fissionsprocessen och bidra till fortsatt utveckling av teoretiska kärnmodeller.

[1]Lund är en av de platser där det bedrivs forskning på detta område, både experimentell och teoretisk. Den experimentella kärnstrukturgruppens lyckade experiment med grundämne 115 behandlas i Ulrika Forsbergs doktorsavhandling [1]. Experimentet fick även stort genomslag i media, en lista över nyhetsartiklar finns på http://www.fysik.lu.se/intranat/organisation/service-info/nyhetsarkiv/nyheter-2013/element-115-news-feed/.

Contents

List of publications and author's contributions

This thesis is based on the following publications, referred to by their Roman numerals:

I α-decay calculations of heavy nuclei using an effective Skyrme interaction

D. E. Ward, B. G. Carlsson, and S. Åberg

Physical Review C 88, 064316 (2013)

My contributions: I wrote the code to calculate the formation amplitudes and α-decay half lives. I performed most of the HFB calculations and all of the α-decay calculations. I produced all figures and tables. I contributed to discussions about the method and the results, and participated in the writing of the manuscript.

II Alpha-particle formation and decay rates from Skyrme–HFB wave functions

D. E. Ward, B. G. Carlsson, and S. Åberg

Physica Scripta 89, 054027 (2014)

My contributions: I modified the formation amplitude code used for paper **I** and performed all calculations. I produced all figures and tables. I wrote the manuscript.

III α-decay spectra of odd nuclei using the effective Skyrme interaction

D. E. Ward, B. G. Carlsson, and S. Åberg

Physical Review C 92, 014314 (2015)

My contributions: I derived the expressions for the formation amplitude when using one-quasiparticle HFB states. I then implemented them as an update to my α-decay code used in papers **I** and **II**. I performed all spherical HFB calculations, and all α-decay calculations. I produced all figures except figure 8. I produced all tables. I wrote the first draft, and contributed to discussions and in the writing of the final manuscript.

IV Structure of superheavy nuclei along decay chains of element 115

Yue Shi, **D. E. Ward**, B. G. Carlsson, J. Dobaczewski, W. Nazarewicz, I. Ragnarsson, and D. Rudolph

Physical Review C 90, 014308 (2014)

My contributions: I performed the particles+rotor calculations and produced figures 2, 7, and 8.

V Nuclear shape evolution based on microscopic level densities

D. E. Ward, B. G. Carlsson, T. Døssing, P. Möller, J. Randrup, and S. Åberg

Submitted to Physical Review C November 15, 2016

My contributions: I wrote the code employed for the random-walk fission dynamics calculations, and performed all of those calculations. I did the fitting of the parameters of the extrapolation formula for the level densities. I produced all figures except figure 1. I wrote the first draft for subsections IIC, IIIA, and for section IV. I contributed to discussions during the writing of the manuscript.

Other publications, not included in this thesis:

Spectroscopy of Element 115 Decay Chains

D. Rudolph, U. Forsberg, P. Golubev, L. G. Sarmiento, A. Yakushev, L.-L. Andersson, A. Di Nitto, Ch. E. Dullmann, J. M. Gates, K. E. Gregorich, C. J. Gross, F. P. Heßberger, R.-D. Herzberg, J. Khuyagbaatar, J. V. Kratz, K. Rykaczewski, M. Schadel, S. Åberg, D. Ackermann, M. Block, H. Brand, B. G. Carlsson, D. Cox, X. Derkx, K. Eberhardt, J. Even, C. Fahlander, J. Gerl, E. Jager, B. Kindler, J. Krier, I. Kojouharov, N. Kurz, B. Lommel, A. Mistry, C. Mokry, H. Nitsche, J. P. Omtvedt, P. Papadakis, I. Ragnarsson, J. Runke, H. Schaffner, B. Schausten, P. Thorle-Pospiech, T. Torres, T. Traut, N. Trautmann, A. Turler, A. Ward, **D. E. Ward**, and N. Wiehl

Physical Review Letters 111, 112502 (2013)

^{48}Ca + ^{249}Bk Fusion Reaction Leading to Element Z=117: Long-Lived α-Decaying ^{270}Db and Discovery of ^{266}Lr

J. Khuyagbaatar, A. Yakushev, Ch. E. Düllmann, D. Ackermann, L.-L. Andersson, M. Asai, M. Block, R. A. Boll, H. Brand, D. M. Cox, M. Dasgupta, X. Derkx, A. Di Nitto, K. Eberhardt, J. Even, M. Evers, C. Fahlander, U. Forsberg, J. M. Gates, N. Gharibyan, P. Golubev, K. E. Gregorich, J. H. Hamilton, W. Hartmann, R.-D. Herzberg, F. P. Heßberger, D. J. Hinde, J. Hoffmann, R. Hollinger, A. Hübner, E. Jäger, B. Kindler, J. V. Kratz, J. Krier, N. Kurz, M. Laatiaoui, S. Lahiri, R. Lang, B. Lommel, M. Maiti, K. Miernik, S. Minami, A. Mistry, C. Mokry, H. Nitsche, J. P. Omtvedt, G. K. Pang, P. Papadakis, D. Renisch, J. Roberto, D. Rudolph, J. Runke, K. P. Rykaczewski, L. G. Sarmiento, M. Schädel, B. Schausten, A. Semchenkov, D. A. Shaughnessy, P. Steinegger, J. Steiner, E. E. Tereshatov, P. Thörle-Pospiech, K. Tinschert, T. Torres De Heidenreich, N. Trautmann, A. Türler, J. Uusitalo, **D. E. Ward**, M. Wegrzecki, N. Wiehl, S. M. Van Cleve, and V. Yakusheva

Physical Review Letters 112, 172501 (2014)

Selected spectroscopic results on element 115 decay chains

D. Rudolph, U. Forsberg, P. Golubev, L. G. Sarmiento, A. Yakushev, L.-L. Andersson, A. Di Nitto, Ch. E. Düllmann, J. M. Gates, K. E. Gregorich, C. J. Gross, R.-D. Herzberg, F. P. Heßberger, J. Khuyagbaatar, J. V. Kratz, K. Rykaczewski, M. Schädel, S. Åberg, D. Ackermann, M. Block, H. Brand, B. G. Carlsson, D. Cox, X. Derkx, K. Eberhardt, J. Even, C. Fahlander, J. Gerl, E. Jäger, B. Kindler, J. Krier, I. Kojouharov, N. Kurz, B. Lommel,

A. Mistry, C. Mokry, H. Nitsche, J. P. Omtvedt, P. Papadakis, I. Ragnarsson, J. Runke, H. Schaffner, B. Schausten, P. Thörle-Pospiech, T. Torres, T. Traut, N. Trautmann, A. Türler, A. Ward, **D. E. Ward**, and N. Wiehl

Journal of Radioanalytical and Nuclear Chemistry 303, 1185 (2015)

Recoil-α-fission and recoil-α-α-fission events observed in the reaction ^{48}Ca + ^{243}Am

U. Forsberg, D. Rudolph, L.-L. Andersson, A. Di Nitto, Ch.E. Düllmann, J.M. Gates, P. Golubev, K.E. Gregorich, C.J. Gross, R.-D. Herzberg, F.P. Hessberger, J. Khuyagbaatar, J.V. Kratz, K. Rykaczewski, L.G. Sarmiento, M. Schädel, A. Yakushev, S. Åberg, D. Ackermann, M. Block, H. Brand, B.G. Carlsson, D. Cox, X. Derkx, J. Dobaczewski, K. Eberhardt, J. Even, C. Fahlander, J. Gerl, E. Jäger, B. Kindler, J. Krier, I. Kojouharov, N. Kurz, B. Lommel, A. Mistry, C. Mokry, W. Nazarewicz, H. Nitsche, J.P. Omtvedt, P. Papadakis, I. Ragnarsson, J. Runke, H. Schaffner, B. Schausten, Y. Shi, P. Thörle-Pospiech, T. Torres, T. Traut, N. Trautmann, A. Türler, A. Ward, **D.E. Ward**, and N. Wiehl

Nuclear Physics A 953, 117 (2016)

How to calculate α-decay rates in the future?

B. G. Carlsson, **D. E. Ward**, and S. Åberg

EPJ Web of Conferences 131, 08002 (2016)

Chapter 1

Introduction

Currently, more than 3300 different nuclides are known from nuclear-physics experiments [2]. Only 288 of these are stable, or have life times comparable to the age of our solar system and can be considered practically stable [3]. This implies that exploring and understanding the decay of atomic nuclei is a central topic in nuclear physics. The atomic nucleus is a many-body quantum system composed of strongly interacting particles, and it can have complex decay properties. While some basic features of nuclear stability can be understood in terms of binding energies, to describe the decay processes in detail, the structure of the nucleus must be taken into account. This thesis is devoted to the theoretical description of the influence of nuclear structure on decay properties of heavy nuclei. α-decay, the emission of a ^{4}He nucleus from an unstable larger nucleus, is considered in the first part, which comprises papers I, II, and III. α-decay is a common decay mode for heavy nuclides, and an important decay mode for superheavy nuclei.

Superheavy nuclei (SHN) are the heaviest nuclei and owe their stability to quantum shell effects [4]. Until the late 1930s the standard view in the scientific community was that the highest atomic number was uranium $Z = 92$ [5]. In 1939 Bohr and Wheeler used their liquid-drop model to describe fission [6]. This model put the upper limit of possible elements at $Z \sim 110$. Myers and Swiatecki discussed in 1966 possible locations of spherical shell closures giving rise to SHN [7]. In detailed calculations in 1969 Nilsson and coworkers [8] predicted an island of stability for SHN around $Z = 114$ and $N = 184$. Superheavy-element research is still an active field today both on the theory side and with experiments to create and study new elements.

All known SHN are unstable and must be synthesized in nuclear reactions. Recent experiments have pushed the limit of observed nuclides to proton number $Z = 118$ [9]. During the writing of this thesis, the International Union of Pure and Applied Chemistry

(IUPAC) announced the names for elements $Z = 113, 115, 117$, and 118: nihonium (Nh), moscovium (Mc), tennessine (Ts), and oganesson (Og) [10]. The observed SHN commonly decay through a chain of α-decays. Different nuclear states in a given nucleus can be populated during these decays, especially when the number of protons and/or neutrons is odd. To better identify, and study the structure of SHN, combined α-decay and nuclear-spectroscopy experiments can be carried out [11, 12]. One motivation for my work on α-decay is to develop theoretical methods to aid in the prediction and interpretation of results from such experiments in collaboration with the experimental nuclear structure group in Lund. Which states are populated during the α-decay can be estimated by approximate selection rules [13], but due to the complexity of the decay process these rules are often very inaccurate. To properly predict the probability of ending up in a given nuclear state requires detailed calculations.

The nucleus is composed of many interacting protons and neutrons, and these particles have in turn internal structure described by the quarks and gluons of the theory of quantum chromodynamics. This makes it practically impossible to describe the nuclear quantum system exactly. One has to choose a model with a suitable level of approximation. The first step is to consider protons and neutrons as structureless particles interacting through effective interactions. The resulting many-body problem can then be treated at different levels of approximation. The goal for the theoretical description is to be able to reasonably predict both static and decay properties using the same model applicable to many different nuclei.

To be able to effectively describe heavy nuclei, systems containing hundreds of particles, a mean-field model can be employed. In this work, a Skyrme-Hartree-Fock-Bogoliubov (SHFB) model is used to describe the α-decaying nuclei. SHFB models can successfully describe many static properties such as binding energies and densities of a large number of heavy nuclei, while not being too costly in terms of computational resources [14]. Due to the general applicability of SHFB models, the possibility to extend these models to include beyond mean-field effects [15, 16], and their adoption to describe other decay properties such as fission [17, 18] and β-decay [19, 20] it is interesting to explore the description of α-decay within this framework.

In paper I, spherical nuclei with even numbers of protons and neutrons are considered. Several aspects of the description of α-decay rates connecting ground states of the decaying parent and resulting daughter nuclei are investigated. In paper II, the effects of using a different SHFB parameterization, and the sensitivity of the decay rate to changing the spatial extent of the α-particle wave function are investigated. Paper III contains results for spherical nuclei with an odd number of nucleons. α-decay leading to different excited states in the daughter nucleus, the hindrance of certain decays and the relation to empirical selection rules are investigated. All three papers contain comparisons with experimental data, and papers I and III contain predictions for α-decay properties of SHN.

The second part of the thesis concerns the description of low-lying states in SHN. Several decay chains of the SHN $^{288}115$ where observed in combined α-decay and spectroscopy experiments performed by D. Rudolph and coworkers of the Lund experimental nuclear structure group [21]. These experiments were the first to resolve different excited states and electromagnetic transitions between these states for several SHN. In paper IV the structure of nuclei in the α-decay chain were investigated using two different models, with the aim of better understanding the experimental results and the constraints they imply on nuclear structure models for this region of the nuclear chart. The models were a SHFB model and a Macroscopic-Microscopic particles+rotor model.

Macroscopic-Microscopic (MM) models can be seen as a further simplification of the many-body problem compared to HFB-models. While HFB treats all nucleons on the same footing, in the MM approach the bulk properties of the nucleus is treated separately from the influence of the least bound nucleons. The bulk contribution to the binding energy is given by a model for a drop of structureless nuclear matter. The least bound nucleons give a correction to the bulk energy obtained by considering an approximate mean field.

To describe excited states when the nucleus is deformed, the particles+rotor model is used. By coupling the odd proton and the odd neutron to the remaining nucleons, approximated as a rotating structureless core, many features of the low-energy part of the excitation spectrum can be described.

The last part of this thesis concerns the influence of nuclear structure on the fission process. It has been shown that a MM model combined with a simple statistical treatment of highly-damped shape evolution gives a good description of observed fragment yields in induced fission [22, 23]. The shape evolution of the excited nucleus is mainly determined by how the number of possible configurations of the nucleus changes with shape. In paper V the fission model is improved by including the microscopically calculated level density at different deformations. The level densities are obtained in a combinatorial model [24] using many-particle-many-hole excitations of the mean-field corresponding to the employed MM model. The nuclear excitations are described using a pairing residual interaction, with blocking taking into account, and include the rotational bands built upon the different quasiparticle configurations.

Chapter 2

SHFB description of heavy nuclei

2.1 Introduction

For the calculations of α-decay properties described in chapter 3, nuclear wave functions for the parent and daughter nuclei are needed as input. To tractably calculate the wave functions for these heavy nuclei, with hundreds of interacting nucleons, approximate treatments are needed. In the α-decay studies, the Skyrme-Hartree-Fock-Bogoliubov (SHFB) approach is chosen.

A wide variety of approaches to describe nuclear structure can be found in the literature, employing different levels of approximation. At one end are the *ab-inito* approaches, e.g. [25–27], where one tries to describe the nucleus at the most basic level allowed by current computational resources. The basic degrees of freedom are chosen to be the protons and neutrons, interacting through realistic nucleon-nucleon potentials. These potentials should describe the scattering of free nucleons and be as closely connected to the underlying theory of quantum chromodynamics as possible. Solving the models requires advanced many-body techniques and large-scale computing, which limits the applicability to lighter nuclei.

At the other end are macroscopic-microscopic approaches, e.g. [8, 28, 29], employed in the studies presented in papers IV and V, and discussed in Chapters 4 and 5. This type of approach can be applied throughout the nuclear chart, and to a relatively low computational cost, but relies heavily on phenomenological modeling.

The SHFB and other similar self-consistent mean-field approaches fall somewhere in between these two categories. With SHFB all nucleons are considered explicitly, but they interact through effective interactions and the type of nucleon correlations allowed are restricted to simplify the calculations. In the Hartree-Fock (HF) approach, nucleons are

described as independent particles, with only the correlations stemming from the Pauli exclusion principle treated explicitly. In the employed Hartree-Fock-Bogoliubov (HFB) approach, the pairing correlations between like nucleons are also included in the wave function by considering independent Bogoliubov quasiparticles. The effective interactions between nucleons is tuned at the mean-field level, so that the solutions give a good description of bulk properties such as binding energies and charge densities.

The approach has many connections to density functional theory for electronic systems, and modern formulations of the SHFB approach are constructed using energy-density-functionals (EDFs) [14, 30, 31], instead of the picture of HFB wave functions and effective interactions. For practical purposes of computation the two pictures are very similar, and in this chapter I will outline the employed SHFB method in the latter picture. The effective-interaction picture is closer to the historical development of the model, but it is not my intention to review these developments. This choice is made in the hope of making the presentation of the method more pedagogical.

This Chapter is organized as follows: Section 2.2 describes the HFB equations obtained when minimizing the energy with an effective interaction. In Sec. 2.3, the Skyrme effective interaction is presented, along with some discussion on the approach. Finally, Sec. 2.4 briefly describes the computational application of the method.

2.2 Hartree Fock Bogoliubov equations

2.2.1 HFB wave function

An HFB wave function can be defined in terms of the quasiparticle operators [32],

$$\beta_k^\dagger = \sum_l U_{lk} a_l^\dagger + V_{lk} a_l, \tag{2.1}$$

where the operator $a_l^\dagger$ creates a particle, and a_l annihilates a particle in state l. The matrices U and V define a unitary transformation from the set of operators $(a, a^\dagger)$ to the set of quasiparticle operators $(\beta, \beta^\dagger)$,

$$\begin{pmatrix} \beta \\ \beta^\dagger \end{pmatrix} = \mathcal{W}^\dagger \begin{pmatrix} a \\ a^\dagger \end{pmatrix}, \tag{2.2}$$

with

$$\mathcal{W} = \begin{pmatrix} U & V^* \\ V & U^* \end{pmatrix}. \tag{2.3}$$

The HFB state $|\mathrm{HFB}\rangle$ is the vacuum to the quasiparticle excitations (2.1),

$$\beta_k |\mathrm{HFB}\rangle = 0, \quad \forall k. \tag{2.4}$$

The benefit of this construction is that the state contains explicitly pairing correlations [33], while retaining the characteristics of a product state, simplifying calculations. The quasiparticles obey fermion commutation relations, together with (2.4) and Wick's theorem [34], this implies that expectation values of operators can be expressed in terms of the *density matrix* $\rho_{ij} = \langle \mathrm{HFB}|a_j^\dagger a_i|\mathrm{HFB}\rangle$, and the *pairing tensor* $\kappa_{ij} = \langle \mathrm{HFB}|a_j a_i|\mathrm{HFB}\rangle$.

The density matrix and pairing tensor defines the state $|\mathrm{HFB}\rangle$ uniquely (up to a phase) [32], and are related to the U and V matrices through $\rho = V^* V^T$, $\kappa = V^* U^T$. A state is an HFB state if and only if the generalized density matrix,

$$\mathcal{R} = \begin{pmatrix} \rho & \kappa \\ -\kappa^* & 1-\rho^* \end{pmatrix}, \tag{2.5}$$

obeys $\mathcal{R}^2 = \mathcal{R}$ [32]. The eigenvalues of $\mathcal{R}$ are thus either 0 or 1. $\mathcal{R}$ is diagonal in the quasiparticle basis,

$$\mathcal{W}^\dagger \mathcal{R} \mathcal{W} = \begin{pmatrix} 0 & 0 \\ 0 & 1 \end{pmatrix}. \tag{2.6}$$

The quasiparticles $\beta^\dagger$ are linear combinations of annihilation and creation operators, and thus do not conserve the number of particles. To get the correct particle number on average, the energy is minimized with a constraint.

2.2.2 Variation of the energy with a two-body interaction

A nuclear Hamiltonian with a two-body interaction can be written,

$$H = \sum_{ij} t_{ij} a_i^\dagger a_j + \frac{1}{4} \sum_{ijkl} \bar{v}_{ijkl} a_i^\dagger a_j^\dagger a_l a_k, \tag{2.7}$$

where t_{ij} is a matrix element of the kinetic energy, and $\bar{v}_{ijkl}$ is an antisymmetrized two-body matrix element of the nucleon-nucleon interaction. To fix the average particle number a Lagrange parameter λ multiplying the particle number operator N is added to H giving $H' = H - \lambda N$.

The expectation value of H' is given by,

$$\begin{aligned} E' = \langle \mathrm{HFB}|H'|\mathrm{HFB}\rangle &= \sum_{ij} (t_{ij} - \lambda \delta_{ij}) \rho_{ji} + \frac{1}{4} \sum_{ijkl} \bar{v}_{ijkl} \left(\kappa_{ij}^* \kappa_{kl} - \rho_{li} \rho_{kj} + \rho_{ki} \rho_{lj} \right) \\ &= \mathrm{Tr}[\left(t - \lambda + \frac{1}{2}\Gamma \right) \rho] - \frac{1}{2} \mathrm{Tr}[\Delta \kappa^*], \end{aligned} \tag{2.8}$$

with the self-consistent particle-hole field $\Gamma_{jk} = \sum_{il} \bar{v}_{jikl}\rho_{li}$, and particle-particle field $\Delta_{ij} = \frac{1}{2}\sum_{kl} \bar{v}_{ijkl}\kappa_{kl}$.

Variation of Eq. (2.8) with respect to the independent matrix elements of ρ and κ, under the constraint $\mathcal{R}^2 = \mathcal{R}$, leads to a condition for a stationary point of the energy [32],

$$[\mathcal{H}, \mathcal{R}] = 0, \tag{2.9}$$

where $\mathcal{H}$ is the generalized mean-field Hamiltonian,

$$\mathcal{H} = \begin{pmatrix} h & \Delta \\ -\Delta^* & -h^* \end{pmatrix}, \tag{2.10}$$

where $h = t + \Gamma - \lambda$. The matrix $\mathcal{R}$ is diagonal in the basis of quasiparticles, Eq. (2.6), so the minimization of Eq. (2.8) amounts to diagonalizing $\mathcal{H}$, leading to the HFB equations,

$$\mathcal{H}\mathcal{W} = \mathcal{W}\begin{pmatrix} E & 0 \\ 0 & -E \end{pmatrix}, \tag{2.11}$$

where E is a diagonal matrix of eigenvalues E_k. This equation is non-linear due to the self-consistent fields. In most situations for even-even nuclei, the lowest-energy solution of Eq. (2.11) has all E_k positive [32].

2.2.3 Qusiparticle states

The Hamiltonian H', expressed in the quasiparticle basis with $\mathcal{W}$ satisfying Eq. (2.11), can be written,

$$H' = \langle \mathrm{HFB}|H'|\mathrm{HFB}\rangle + \sum_k E_k \beta_k^\dagger \beta_k + H'_{\mathrm{int}}, \tag{2.12}$$

where H'_{int} contains products of four quasiparticle operators. Terms containing $\beta\beta$ and $\beta^\dagger\beta^\dagger$ vanish at the stationary point. This form corresponds to arranging H' in normal order with respect to the solution $|\mathrm{HFB}\rangle$ in the sense of Wick's theorem [34]. The term H'_{int} contains uncontracted products of operators and is similar to a two-body interaction among quasiparticles. If one neglects this term H' has eigenstates $|\mathrm{HFB}\rangle$ and $\beta_k^\dagger|\mathrm{HFB}\rangle$, with excitation energies 0 and E_k, respectively. The eigenvalues E_k are thus called quasiparticle energies. For an even-even vacuum $|\mathrm{HFB}\rangle$, the one-quasiparticle states $\beta_k^\dagger|\mathrm{HFB}\rangle$ define approximate HFB wave functions for states in neighboring odd-A nuclei.

2.3 Skyrme energy density

2.3.1 Effective interaction

As mentioned in the Sec. 2.1, the correlations in the HFB wave functions are limited by construction, and an effective interaction is used. The Skyrme effective interaction used in the calculations is perhaps best motivated by considering the energy density, see subsection 2.3.6 below. An alternative view is to consider it as an approximation to an effective interaction tuned to a class of model wave functions.

Several methods employing model wave functions and effective interactions are employed in no-core shell model calculations [25, 35]. In these calculations, the nucleon correlations are limited by expanding the nuclear wave function in a truncated basis of Slater determinants, the model space. For this limited model space, an effective-interaction Hamiltonian H_{eff} is introduced. Formally, one can define a similarity transformation e^{-S} taking an eigenstate $|\Psi_n\rangle$ of the exact Hamiltonian H, with eigenvalue E_n, to a state in the model space $|\Phi_n\rangle$ [35],

$$|\Phi_n\rangle = e^{-S}|\Psi_n\rangle. \tag{2.13}$$

The effective Hamiltonian $H_{\text{eff}} = e^{-S}He^{S}$ acting on $|\Phi_n\rangle$ then gives the exact eigenvalue E_n. H_{eff} contains in general one-, two-, three- and higher-body operators. To determine the effective interaction exactly is a formidable problem. In practice one must use approximate effective interactions. This can be done at various levels of approximation starting from a realistic nucleon-nucleon interaction [35].

For HFB calculations, one wants an effective interaction so that the ground-state energy can be approximated by minimizing the expectation value $E[\Phi]$,

$$E[\Phi] = \langle\Phi|H_{\text{eff}}|\Phi\rangle, \tag{2.14}$$

with the model wave functions $|\Phi\rangle = |\text{HFB}\rangle$, which are varied as in Sec. 2.2. The effective interaction used in Eq. (2.14) should absorb most of the correlation effects not included in the HFB wave functions. Most importantly, the effective interaction should remove the strong repulsion at short ranges in the bare nucleon-nucleon interaction. One *ab-inito* approach to obtain an effective interaction to use in Eq. (2.14) is the Brückner G-matrix approach [36, 37]. Another more recent approach, allowing to make systematic approximations for the effective interaction, is the method of low-momentum effective interactions [38]. Both approaches have been employed in recent studies, e.g. [39, 40], on how to move towards *ab-inito* mean-field models for heavy nuclei. However, presently phenomenological approaches need to be employed to successfully describe nuclei across the nuclear chart. One starting point for a such a description is to postulate the form of the effective interaction with the strengths of the various terms as free parameters. These

free parameters are then fitted so that binding energies, radii and other bulk properties of heavy nuclei are reproduced.

2.3.2 Skyrme effective interaction

The original Skyrme interaction [41] is a phenomenological effective interaction describing the strong-force interactions between nucleons. It contains two-body terms which have the form of expansions in the relative momentum of the colliding and scattered nucleons up to second order. It also has a three-body contact interaction term, which is equivalent to a density dependent two-body interaction in HF calculations for even-even nuclei [42]. The interaction obeys the symmetries of a general strong-force interaction, e.g., it is invariant under exchange of identical particles, rotations, parity, isospin, and obeys translational and Galilean invariance.

The position-spin matrix element of the Skyrme interaction used for this work reads [43],

$$\begin{aligned}
&\langle \vec{r}_1' s_1' \vec{r}_2' s_2' | \hat{V} | \vec{r}_1 s_1 \vec{r}_2 s_2 \rangle \\
&= \langle s_1' s_2' | \left\{ t_0 \left(1 + x_0 P^\sigma\right) + \frac{1}{2} t_1 \left(1 + x_1 P^\sigma\right) \left[\vec{k}'^2 + \vec{k}^2 \right] \right. \\
&+ t_2 \left(1 + x_2 P^\sigma\right) \vec{k}'^* \cdot \vec{k} + \frac{1}{6} t_3 \left(1 + x_3 P^\sigma\right) \left[\rho_0 \left(\frac{\vec{r}_1 + \vec{r}_2}{2} \right) \right]^\alpha \\
&\left. + i W_0 \vec{S} \cdot \left(\vec{k}'^* \times \vec{k} \right) \right\} | s_1 s_2 \rangle \delta(\vec{r}_1' - \vec{r}_1) \delta(\vec{r}_2' - \vec{r}_2) \delta(\vec{r}_1 - \vec{r}_2),
\end{aligned} \tag{2.15}$$

where P^σ is the spin-exchange operator,

$$\langle s_1' s_2' | P^\sigma | s_1 s_2 \rangle = \delta_{s_1' s_2} \delta_{s_2' s_1}, \tag{2.16}$$

and $\vec{S}$ is the spin operator,

$$\langle s_1' s_2' | \vec{S} | s_1 s_2 \rangle = \vec{\sigma}_{s_1' s_1} \delta_{s_2' s_2} + \delta_{s_1' s_1} \vec{\sigma}_{s_2' s_2}, \tag{2.17}$$

where $\vec{\sigma} = (\sigma^x, \sigma^y, \sigma^z)$ are vectors of Pauli spin matrices. The relative-momentum operators $\vec{k} = \frac{1}{2i} (\nabla_1 - \nabla_2)$ and $\vec{k}' = \frac{1}{2i} (\nabla_1' - \nabla_2')$ act on the δ-functions in the sense of distributions. $\rho_0(\vec{R}) = \rho_\mathrm{p}(\vec{R}) + \rho_\mathrm{n}(\vec{R})$ is the sum of the proton and neutron local densities. The parameters of the interaction are $t_0, t_1, t_2, t_3, x_0, x_1, x_2, x_3, W_0$, and α. The power α of the density dependence generalizes the density dependence $\alpha = 1$ found with the original Skyrme force, and a smaller power between $1/6$ and $1/3$ is generally used [14].

2.3.3 Pairing interaction

The HFB energy depends on the particle-hole (ph) mean field Γ and the particle-particle (pp) mean field Δ, c.f. Eq. (2.8). In order to obtain a simple description of the pairing

properties, the effective interaction generating the pp field is parametrized differently from the ph interaction. A commonly used parameterization for SHFB calculations is [14],

$$\hat{V}^{q}_{\text{pair}} = V_q \left(\frac{1-P^\sigma}{2}\right)\left[1 - d\left(\frac{\rho_0(\vec{r}_1)}{\rho_{\text{sat}}}\right)\right]\delta(\vec{r}_1 - \vec{r}_2), \tag{2.18}$$

where $q = \text{n(p)}$, refers to neutrons(protons), $\rho_{\text{sat}} = 0.16\ \text{fm}^{-3}$ is the saturation density, and d is a unitless parameter controlling the density dependence. This interaction has the form of a Skyrme interaction with only t_0 and t_3 terms. It only contributes in the isovector-spin-singlet channel, for two like particles the protons or neutrons must have anti-parallel spin projections. The interaction (2.18) is used in the calculations presented in papers I-III. Pairing between protons and neutrons is not considered. The coulomb repulsion between two protons is also not included explicitly in the pp channel, but is taken account through different coupling constants for protons V_{p} and neutrons V_{n}.

If the interaction (2.18) or another Skyrme interaction is used in the particle-particle channel, a cutoff to prevent divergences in the pairing energy is needed [14]. In papers I-III the truncation is performed using the equivalent-spectrum method [44].

2.3.4 Coulomb interaction

The Coulomb interaction is approximated by considering Coulomb interactions only in the particle-hole channel and using the Slater approximation [45] for the exchange term when calculating the expectation value of the Coulomb energy,

$$E_{\text{Coul}} = \frac{e^2}{2}\int d\vec{r}d\vec{r}'\frac{\rho_{\text{p}}(\vec{r})\rho_{\text{p}}(\vec{r}')}{|\vec{r}-\vec{r}'|} - \frac{3e^2}{4}\left(\frac{3}{\pi}\right)^{1/3}\int d\vec{r}\left[\rho_{\text{p}}(\vec{r})\right]^{4/3}. \tag{2.19}$$

2.3.5 Rearrangement potentials

In the employed SHFB approach, with different density-dependent effective interactions in the particle-hole (ph) and particle-particle (pp) channels, the expectation value of the energy, Eq. (2.8), should be modified,

$$E' = \sum_{ij}(t_{ij} - \lambda\delta_{ij})\rho_{ji} + \frac{1}{4}\sum_{ijkl}\overline{v}^{(\text{pp})}_{ijkl}[\rho]\kappa^*_{ij}\kappa_{kl} + \overline{v}^{(\text{ph})}_{ijkl}[\rho]\left(\rho_{ki}\rho_{lj} - \rho_{li}\rho_{kj}\right). \tag{2.20}$$

The mean-fields in Eqs. (2.9-2.11) obtained from variation are given by,

$$h_{ij} = \frac{\delta E'}{\delta\rho_{ji}}, \quad \Delta_{ij} = \frac{\delta E'}{\delta\kappa^*_{ij}}. \tag{2.21}$$

The ph mean-field h will contain additional terms due to the density dependence of both $\bar{v}^{(\mathrm{pp})}_{ijkl}[\rho]$ and $\bar{v}^{(\mathrm{ph})}_{ijkl}[\rho]$, called rearrangement potentials.

2.3.6 Energy density

The expectation value of the energy with the Skyrme interaction leads to an expression involving energy-density functionals,

$$\langle \mathrm{HFB}|H|\mathrm{HFB}\rangle = T + \int d\vec{r}\mathcal{E}_{\mathrm{Skyrme}}(\vec{r}) + \int d\vec{r}\mathcal{E}_{\mathrm{pair}}(\vec{r}) + E_{\mathrm{Coul}}, \tag{2.22}$$

where T and E_{Coul} are the expectation values of the kinetic and Coulomb energies respectively. The functionals are integrals over the energy densities $\mathcal{E}(\vec{r})$, which are functions of local densities and derivatives of local densities up to second order.

An energy-density functional (EDF) with a similar form as $\int d\vec{r}\mathcal{E}_{\mathrm{Skyrme}}(\vec{r})$ can also be obtained from a finite-range interaction using a density matrix expansion (DME). The DME includes expanding the density $\rho(\vec{r}_1, \vec{r}_2)$ in the relative coordinate $\vec{r} = \vec{r}_1 - \vec{r}_2$, around the local density $\rho(\vec{r}_1)$ [14]. Negele and Vautherin [46] showed that an energy density similar to what is obtained with the Skyrme interaction arises when performing a variant of DME. They considered the energy density in the HF approach with an effective interaction obtained from a realistic nucleon-nucleon interaction, and expanded up to second order in derivatives. The density expansion is done in a way so it contains the behavior of the exact infinite nuclear-matter density in the first order. The energy functional is thus a local density approximation with corrections due to finite size effects. The similarity of this more realistic energy density with the Skyrme energy density provides a motivation for the Skyrme interaction.

It also shows that the Skyrme interaction (2.15) is not a pure low-momentum expansion of an effective interaction. Realistic effective interactions should contain the long-range one-pion exchange part, which cannot be approximated by its momentum-space Taylor series when comparing with typical Fermi momenta k_{F} [47]. The long-range part is instead absorbed in the coupling constants of the functional obtained with the DME [46].

A more flexible formulation of the SHFB approach is obtained if one starts from an EDF, $E = \int d\vec{r}\mathcal{E}(\vec{r})$, instead of with the effective interaction. In the context of energy-density functionals, the energy density can have different density dependences than obtained with the original Skyrme interaction. In this way one can better motivate the non-integer power of the density dependence in the effective interaction (2.15), and the use of different interactions in the particle-hole and particle-particle channels, c.f. Eq. (2.20). The coupling constants appearing in $\mathcal{E}(\vec{r})$, which are more numerous than the number of Skyrme force

parameters, also need not to obey the same interrelations as with the Skyrme interaction (2.15) [30].

2.4 Solving the HFB equations

In papers I-III spherical nuclei were considered. The HFB equations are restricted to spherical symmetry and solved using the code HOSPHE [48] in an updated version developed by B. G. Carlsson, J. Toivanen, and Yue Shi. The HFB quasiparticles, Eq. (2.1), are expanded in the spherical-harmonic-oscillator (SHO) basis [49]. The basis is truncated to include all single-particle states with major oscillator quantum number $N \leq N_{\max}$.

Equation (2.11) is solved by iterative diagonalization. The iterations are started with an initial guess for the densities ρ and κ. An iteration then consists of the steps:

1. Use the densities obtained in the previous iteration to compute the mean fields h and Δ represented as matrices in the SHO basis. The matrix elements of the mean-fields are efficiently computed using the coordinate-space representation. With the Skyrme interaction and the spherical symmetry, the needed matrix elements can be expressed as radial integrals over products of one-dimensional functions, and evaluated using numerical quadrature [48].
2. Diagonalize $\mathcal{H}$, c.f. Eq. (2.11), to obtain U and V matrices.
3. Construct new densities ρ and κ from the U and V matrices. The quasiparticles with positive eigenvalues E are used.
4. If a convergence criteria for the total energy is met, stop the iteration, otherwise repeat steps 1.-4.

2.4.1 Avoiding collapse of the pairing correlations

When the strength of the pairing interaction (2.18) is weak compared to the energy spacing of the HF single-particle levels, the pairing correlations collapse and the solution to the HFB equations becomes an uncorrelated HF determinant. This typically happens when considering a closed shell nucleus such as ^{208}Pb. For a nucleus, which is a finite quantum system, this sharp pairing phase transition should not occur.

In models employing more complicated trial wave functions pairing correlations are present, but smaller in magnitude, also for closed shell nuclei. An extension of the HFB approach, where the collapse of the pairing is absent, and where the trial wave functions have good

particle number, is the variation-after-projection (VAP) method. The trial wave function in the VAP approach is the projection of a HFB state onto good particle number, which is then varied. This extension is unfortunately much more costly in terms of computation.

To avoid the collapse of the pairing in the HFB calculations, the Lipkin-Nogami method [44] is used instead. The Lipkin-Nogami (LN) approach [50, 51] corresponds to an approximate variation after projection [52]. In the LN approach an additional term is added to the effective Hamiltonian, which becomes,

$$H' = H - \lambda_1 N - \lambda_2 N^2. \tag{2.23}$$

The λ_2 term arises as a correction term to the energy when using particle-nonconserving wave functions [50]. Its value is determined through an auxiliary equation and changes during the HFB iterations [44].

Chapter 3

Model for α-decay

Introduction

α-decay is the process of an unstable mother nucleus splitting into an α particle (a ^{4}He nucleus), and a daughter nucleus. The decay process consists of the four nucleons making up the α particle clustering together and then escaping, leaving the daughter nucleus, see Fig. 3.1. In the work presented in this thesis this process is modeled microscopically by considering interacting nucleons as the basic degrees of freedom.

The Q_α value measures the difference in binding energy of the mother nucleus in its initial state, E_{M}, and the sum of the binding energies for the daughter and α particle, E_{D} and E_α,

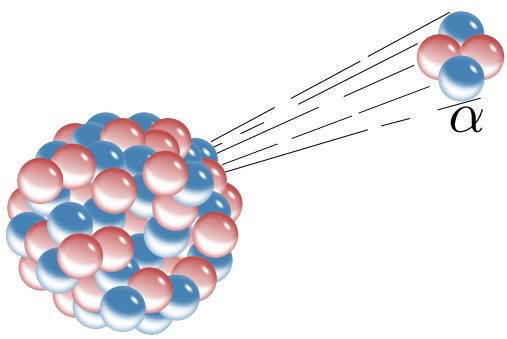

Figure 3.1: Artist's rendition of α-decay. The figure is taken from [53], and is in the public domain.

in their respective states after the split,

$$Q_\alpha = E_\mathrm{M} - E_\mathrm{D} - E_\alpha. \tag{3.1}$$

When the two fragments are far apart, the energy Q_α becomes the kinetic energy of the relative motion with the reduced mass $\mu = \frac{m_\alpha m_\mathrm{D}}{m_\alpha + m_\mathrm{D}}$. For a mother nucleus at rest in the laboratory, Q_α is the sum of the daughter nucleus recoil energy and the α-particle kinetic energy. The total angular momentum I_M and parity π_M are conserved during the decay. The total system after the split can be described by the internal daughter nucleus wave function, with angular momentum I_D and parity π_D, the internal alpha particle wave function which has $I^\pi = 0^+$, and the relative motion part. The relative motion can be decomposed in partial waves with angular momentum l_α, and parity $\pi = (-1)^{l_\alpha}$. The conservation of angular momentum and parity then implies that the triangular rule $|I_M - I_D| \leq l_\alpha \leq I_M + I_D$ should be obeyed, and only even or odd partial waves are allowed according to $(-1)^{l_\alpha} = \pi_D \pi_M$.

The investigated α-decays start from the ground-state or a low-lying state in the mother nucleus. This implies that the α particle must escape a high Coulomb barrier through quantum-mechanical tunneling. This leads to half-lives $T_{1/2} > 10^{-10}$ s, that are many orders of magnitude longer than typical nucleon time scales, e.g. the classical period of oscillation of a nucleon inside the nuclear mean field $t \approx 10^{-22}$ s. In a semi-classical picture, the α-particle bounces against the inside of the Coulomb barrier a very large number of times before tunneling through. The initial mother nucleus state is thus almost stationary.

The initial state can be described using a Gamow state [54], see Sec. 3.1.1. With a slow decay rate the Gamow state becomes very similar to a bound state inside and well into the Coulomb barrier. The decay rate depends on the nuclear wave function in the Coulomb barrier, a small fraction of the wave function tail penetrates the barrier leading to the tunneling. The part of the wave function governing the α-decay is the part composed of the daughter nucleus and α particle. The magnitude of this component, or *formation amplitude,* depends on the overlap of the mother nucleus wave function with that of the combined α-cluster and daughter wave function, and is sensitive to the nuclear structure.

The flow of α-particle probability passing through the Coulomb barrier is exponentially sensitive to the decay energy, so the most important quantity determining the half life is the Q_α value. For the decay of odd nuclei, several daughter nucleus states can be accessible with only small differences in Q_α values. In this case the differences in formation amplitude can play a large role in determining the decay paths. In the formalism employed in this work the decay rate is divided into two factors, one containing the formation amplitude and one containing the energy-dependent barrier penetrability. This is similar to the division of the electromagnetic quadrupole transition rate where the $B(E2)$ value contains the effect of nuclear structure, and another factor contains the strong energy dependence.

This chapter is organized in the following way: Sec. 3.1 presents the theory for the microscopic description of α-decay, Sec. 3.2 outlines the calculation of the formation amplitudes using SHFB wave functions, Sec. 3.3 includes a summary of some of the results using this approach, and finally Sec. 3.4 contains an outlook on further developments.

3.1 Theory

The decay formalism used is the microscopic approach to cluster emission reviewed in Refs. [55, 56]. The calculations follow essentially what is denoted "BCS approach to α-decay" in Ref. [55], but instead the HFB wave functions described in chapter 2 are used.

The approach is based on the time-independent Schrödinger equation in the coordinate representation of the inter-fragment distance r. An approximation for the decay width can be derived using tools from R-matrix theory [57], as done for instance in the pioneering work of Thomas [58], and in the review [55]. Exponential decay can be described using Gamow states [54, 59, 60], and the concept of an exponential time dependence can be used as the basis for the derivation of the microscopic description of α decay [61, 62]. Both approaches result in similar expressions for the decay width. I consider the latter formulation more instructive, so in the following sections I will describe the formalism following the literature using this latter picture. A similar shorter outline of the theory was included in paper I. Here some more details are included, which I hope can be useful for students and non-specialists.

3.1.1 Gamow states for α decay

Gamow states generalize the solution of the time-independent Schrödinger equation to complex energies,

$$H|\Psi\rangle = E|\Psi\rangle = (E_{\mathrm{r}} - i\frac{\Gamma}{2})|\Psi\rangle, \tag{3.2}$$

where E_{r} is the real part, and $-\Gamma/2$ the imaginary part of the energy E. With a complex energy, the time dependence of the state $|\Psi(t)\rangle$,

$$|\Psi(t)\rangle = e^{-iHt/\hbar}|\Psi\rangle = e^{-iE_{\mathrm{r}}t/\hbar}e^{-\Gamma t/2\hbar}|\Psi\rangle, \tag{3.3}$$

implies an exponential decay of probabilities when $\Gamma > 0$, as the time dependence is governed by

$$|e^{-iE_{\mathrm{r}}t/\hbar}e^{-\Gamma t/2\hbar}|^2 = e^{-\Gamma t/\hbar}. \tag{3.4}$$

An introduction to Gamow states, and their physical interpretation can be found in Ref. [63].

If the daughter nucleus and α particle can be approximated as point particles interacting through a local potential $V(r)$, Eq. (3.2) can be written,

$$\frac{d^2u_l(r)}{dr^2} = \left[\frac{l(l+1)}{r^2} + \frac{2\mu}{\hbar^2}(V(r) - E)\right] u_l(r), \tag{3.5}$$

where r is the distance between the particles, μ is the reduced mass, and l is the angular momentum associated with their relative motion. $u_l(r)$ is the partial wave function, appearing in the following decomposition of the wave function $\psi(\vec{r})$,

$$\psi(\vec{r}) = \sum_l R_l(r)\, Y_{lm}(\hat{r}) = \sum_l \frac{u_l(r)}{r}\, Y_{lm}(\hat{r}), \tag{3.6}$$

where the $Y_{lm}(\hat{r})$ are spherical harmonics. At long distances the nuclear interaction vanishes and only the Coulomb interaction remains. In terms of the wavenumber $\kappa = \frac{\sqrt{2\mu E}}{\hbar}$; Sommerfeld parameter $\eta = \frac{Z_\alpha Z_D e^2 \mu}{\hbar^2 \kappa}$, where $Z_{\alpha(D)}$ is the charge of the α particle(daughter nucleus); and the dimensionless radius $\rho = \kappa r$, the radial equation (3.5) then becomes,

$$\frac{d^2u_l(\rho)}{d\rho^2} = \left[\frac{l(l+1)}{\rho^2} + \frac{2\eta}{\rho} - 1\right] u_l(\rho). \tag{3.7}$$

The regular and irregular Coulomb wave functions, $F_l(\eta, \rho)$ and $G_l(\eta, \rho)$, are solutions to this equation [64, 65]. The linear combinations

$$H_l^{(\pm)}(\eta, \rho) = G_l(\eta, \rho) \pm iF_l(\eta, \rho), \tag{3.8}$$

behave asymptotically as

$$H_l^{(\pm)}(\eta, \rho) \xrightarrow[\rho\to\infty]{} \exp\left[\pm i(\rho - \frac{1}{2}l\pi - \eta\ln(2\rho) + \sigma_l)\right], \tag{3.9}$$

where σ_l is the Coulomb phase shift [57]. Thus, far away from the origin the solutions $H^{(\pm)}$ will behave as outgoing $(+)$ or incoming $(-)$ spherical waves. The phase $-\eta\ln(2\rho) + \sigma_l$ comes from the Coulomb interaction, which is felt even at large distances.

For scattering problems the following asymptotic form can be used [56, 57],

$$u_l(r) \to C_l\left[H_l^{(-)}(\eta, \rho) - S_l(E)H_l^{(+)}(\eta, \rho)\right], \tag{3.10}$$

where C_l is a normalization constant, and the scattering matrix $S_l(E)$ has modulus 1 for real energies. $S_l(E) = 1$ corresponds to pure-Coulomb (Rutherford) scattering, while the nuclear interactions can cause additional scattering giving $S_l(E) \neq 1$ [57].

Gamow states with $\Gamma > 0$ can be obtained by imposing a boundary condition of a purely outgoing state,

$$u_l(r) \xrightarrow[r\to\infty]{} u_l^{\text{as}}(r) \propto H_l^{(+)}(\eta, \kappa r), \tag{3.11}$$

on the solutions of Eq. 3.5. This boundary condition is only satisfied by a discrete set of complex energies E, corresponding to resonance poles of the scattering matrix $S_l(E)$ [56].

With the complex energy $E = E_r - i\Gamma/2$, the wave number κ becomes complex,

$$\kappa = \sqrt{2\mu E}/\hbar = \Re(\kappa) + i\Im(\kappa), \tag{3.12}$$

with the real part $\Re(\kappa) > 0$ and the imaginary part $\Im(\kappa) < 0$ for a decaying state with purely outgoing boundary conditions [56, 63]. The imaginary part $\Im(\kappa)$ will modulate the amplitude of the outgoing wave,

$$|u_l^{\text{as}}(r)| \approx e^{-\Im(\kappa)r}, \tag{3.13}$$

causing an increase in amplitude with increasing distance. This increase is interpreted as coming from the larger number of particles situated at smaller radii at earlier times (due to the decay), which have then traveled out from the origin to the point r [63].

3.1.2 Current expression for decay width

The decay width Γ can be extracted from the probability current passing through the surface of a sphere. For the Gamow state (3.6) the rate of decrease of the probability density within a volume V at time $t = 0$ is given by,

$$\frac{\partial}{\partial t}\int_V d\vec{r}\psi^*(\vec{r},t)\psi(\vec{r},t)\bigg|_{t=0} = \frac{-\Gamma}{\hbar}\int_V d\vec{r}\psi^*(\vec{r})\psi(\vec{r}). \tag{3.14}$$

The same quantity can be calculated using the Schrödinger equation,

$$\begin{aligned}
&\frac{\partial}{\partial t}\int_V d\vec{r}\psi^*(\vec{r},t)\psi(\vec{r},t)\bigg|_{t=0} \\
&= -\frac{i\hbar}{2\mu}\int_V d\vec{r}\nabla\cdot(\psi\nabla\psi^* - \psi^*\nabla\psi) \\
&= -\frac{i\hbar}{2\mu}\int_{r=r_V} r^2\sin\theta d\theta d\phi\left(\psi\frac{\partial\psi^*}{\partial r} - \psi^*\frac{\partial\psi}{\partial r}\right) \\
&= -\frac{i\hbar}{2\mu}\sum_l r_V^2\left(R_l\frac{\partial R_l^*}{\partial r} - R_l^*\frac{\partial R_l}{\partial r}\right)_{r=r_V},
\end{aligned} \tag{3.15}$$

where r_V is the radius of the sphere defining the volume V, and for the second line it is assumed that the potential $V(r)$ is real. Comparing Eqs. (3.14) and (3.15), and choosing the normalization

$$\int_V d\vec{r}\psi^*(\vec{r},t)\psi(\vec{r},t)\Big|_{t=0} = 1, \tag{3.16}$$

a current expression for Γ is obtained,

$$\Gamma = \frac{i\hbar^2}{2\mu}\sum_l r_V^2\left(R_l\frac{\partial R_l^*}{\partial r} - R_l^*\frac{\partial R_l}{\partial r}\right)_{r=r_V}. \tag{3.17}$$

Beyond the range of inter-fragment nuclear forces the partial waves $u_l(r)$ assume the form of outgoing Coulomb wave functions giving the radial wave functions $R_l(r) \propto H_l^{(+)}(\eta,\kappa r)/r$. In the following, r_V is assumed to be in this region, where only Coulomb forces act between the fragments. Given a radial wave function valid in the interior and out to r_V, $R_l^{(\mathrm{int})}(r)$, the amplitude of the Coulomb wave can be determined,

$$R_l(r) = C_l(r_V)H_l^{(+)}(\eta,\kappa r)/r, \tag{3.18}$$

where $C_l(r_V)$ is the matching constant,

$$C_l(r_V) = r_V\frac{R_l^{(\mathrm{int})}(r_V)}{H_l^{(+)}(\eta,\kappa r_V)}. \tag{3.19}$$

If the decay width Γ is small, the small imaginary part of the wavenumber κ can be neglected if r_V is not too large. When κ is real the probability current through the sphere given by r_V is the same as through any larger sphere around the origin. Using the asymptotic form (3.9), Eq. 3.17, can be simplified,

$$\Gamma = \sum_l \frac{\hbar^2\kappa}{\mu}|C_l(r_V)|^2. \tag{3.20}$$

If the interior solution is exact, $rR_l^{(\mathrm{int})}(r)$ will be proportional to the outgoing Coulomb wave function for radii beyond the nuclear forces, and the decay width given by Eq. (3.20) will not be sensitive to the choice of matching radius r_V. Using an approximate interior solution might introduce a dependence on r_V, and one has to check the sensitivity of the results to the choice of matching radius.

3.1.3 Microscopic description

In the microscopic description of α decay, the mother nucleus, daughter nucleus and α cluster are described by many-body wave functions. The mother-nucleus wave function

should approximate a Gamow state $|\Psi^{(M)}_{I_M M_M}\rangle$, with nuclear spin I_M and projection M_M, satisfying $H|\Psi^{(M)}_{I_M M_M}\rangle = (E_r - i\Gamma/2)|\Psi^{(M)}_{I_M M_M}\rangle$. An appropriate coordinate representation for α decay is,

$$\Psi^{(M)}_{I_M M_M}(x_D, x_\alpha, \vec{r}), \tag{3.21}$$

where x_D represents the internal coordinates for the daughter nucleus, x_α the internal coordinates of the α cluster, and $\vec{r}$ the vector between the center of mass of the daughter and α cluster. Internal coordinates are the Jacobi coordinates corresponding to distances between nucleons and the spin and isospin coordinates of the nucleons. The daughter state for a given α-decay channel k is represented by $\Psi^{(D)}_k(x_D)$, where k contains the spin I_D and projection M_D as well as other quantum numbers to label this state. The α cluster is represented by $\Phi^{(\alpha)}_{00}(x_\alpha)$ describing the ^{4}He ground state with $I = M = 0$.

The following representation of the nuclear Hamiltonian is useful for the description of the decay,

$$H = H_\alpha + H_D - \frac{\hbar^2}{2\mu}\nabla^2_{\vec{r}} + V_{\alpha D}(x_D, x_\alpha, \vec{r}), \tag{3.22}$$

where the first two terms give the energy of the two subsystems,

$$H_\alpha \Phi^{(\alpha)}_{00}(x_\alpha) = E_\alpha \Phi^{(\alpha)}_{00}(x_\alpha), \tag{3.23}$$

$$H_D \Psi^{(D)}_k(x_D) = E_{D,k} \Psi^{(D)}_k(x_D). \tag{3.24}$$

The third term in (3.22) corresponds to the kinetic energy of the relative motion of the two fragments, and the last term the inter-fragment interaction.

The decay width Γ is assumed to arise only from α-decay contributions, generated by the two-cluster component of the mother nucleus,

$$\Psi^{(M)}_{I_M M_M} \sim \sum_{k,l_k} \mathcal{A}_{\alpha D} R_{kl_k}(r) \Psi^{(D\alpha)}_{kl_k}(x_D x_\alpha \hat{r}), \tag{3.25}$$

where $\Psi^{(D\alpha)}_{kl_k}$ is the cluster-angular function,

$$\Psi^{(D\alpha)}_{kl_k}(x_D x_\alpha \hat{r}) = \left[\Psi^{(D)}_k(x_D), \Phi^{(\alpha)}_{00}(x_\alpha) Y_{l_k}(\hat{r})\right]_{I_M M_M}. \tag{3.26}$$

The bracket denotes coupling of angular momentum of the daughter state, I_D, and of the relative motion, l_k, to that of the mother nucleus. The operator $\mathcal{A}_{\alpha D}$ antisymmetrizes the product of the radial function $R_{kl_k}(r)$ and the two internally antisymmetric wave functions $\Psi^{(D)}_k$ and $\Phi^{(\alpha)}_{00}$ by exchanging coordinates. It contains the normalization factor $\mathcal{N}^{-1/2} = \binom{N_M}{2}^{-\frac{1}{2}} \binom{Z_M}{2}^{-\frac{1}{2}}$ preserving the normalization of the cluster angular functions,

$$\int dx_D dx_\alpha d\hat{r} \Psi^{(D\alpha)*}_{kl_k}(x_D x_\alpha \hat{r}) \Psi^{(D\alpha)}_{k'l'_k}(x_D x_\alpha \hat{r}) = \delta_{kk'}\delta_{ll'_k}, \tag{3.27}$$

when the fragments (D) and (α) are separated far enough apart to not have any spatial overlap.

It is assumed that beyond some separation $r > r_0$, the Hamiltonian (3.22) does not mix the cluster component (3.25) with the other components of the mother-nucleus wave function, and that the following coordinate-space Schrödinger equation then holds,

$$H\sum_{k,l_k}\mathcal{A}_{\alpha D}R_{kl_k}(r)\Psi^{(D\alpha)}_{kl_k}(x_Dx_\alpha\hat{r}) = E\sum_{k,l_k}\mathcal{A}_{\alpha D}R_{kl_k}(r)\Psi^{(D\alpha)}_{kl_k}(x_Dx_\alpha\hat{r}). \tag{3.28}$$

Considering the case where the fragments have no spatial overlap, and acting on Eq. (3.28) from the left with

$$\int dx_D dx_\alpha d\hat{r}\Psi^{(D\alpha)*}_{kl_k}(x_Dx_\alpha\hat{r}) \tag{3.29}$$

gives,

$$\frac{d^2u_{kl_k}(r)}{dr^2} = \left[\frac{l_k(l_k+1)}{r^2} - \frac{2\mu}{\hbar^2}Q_k\right]u_{kl_k}(r) + \frac{2\mu}{\hbar^2}\sum_{k'l'_k}V_{kl_k;k'l'_k}(r)u_{k'l'_k}(r), \tag{3.30}$$

where $Q_k = E - E_{D,k} - E_\alpha$ and, $V_{kl;k'l'_k}(r)$ is a potential matrix,

$$\begin{aligned} V_{kl_k;k'l'_k}(r) = &\int dx_D dx_\alpha d\hat{r}\Psi^{(D\alpha)*}_{kl_k}(x_Dx_\alpha\hat{r}) \\ &\times V_{\alpha D}(x_D, x_\alpha, \vec{r})\Psi^{(D\alpha)}_{k'l'_k}(x_Dx_\alpha\hat{r}). \end{aligned} \tag{3.31}$$

If the α particle is beyond the range of the strong-force interaction, $V_{\alpha D}(x_D, x_\alpha, \vec{r})$ only contains Coulomb terms. For spherical mother and daughter nuclei, only the diagonal term in the potential matrix is important,

$$V_{kl_k;kl_k}(r) = \frac{Z_\alpha Z_D e^2}{r}. \tag{3.32}$$

Without the off-diagonal terms of the potential matrix, the different channels kl_k decouple and Eq. (3.30) assumes the form of the radial equation for point-like particles, Eq. (3.5), in each channel. A current expression for the decay width can then be obtained, as described below.

The mother nucleus wave function is normalized to 1 within the sphere defined by $r = r_V$,

$$\int_{r\leq r_V} r^2dr\int dx_D dx_\alpha d\hat{r}|\Psi^{(M)}_{I_MM_M}(x_D, x_\alpha, \vec{r})|^2 = 1. \tag{3.33}$$

Using that the potential terms in the Hamiltonian (3.22) are real, and that the wave function $\Psi^{(M)}_{I_MM_M}$ is normalizable in the cluster angular coordinates $x_Dx_\alpha\hat{r}$, the derivation in Eqs.

(3.14-3.20) can be repeated. The result is that the decay width can be calculated using the current expression (3.20), employing the amplitudes of the radial functions $R_{kl_k}(r)$ in the cluster component of the mother nucleus, Eq. (3.25).

The amplitude in a given channel kl_k is extracted through an overlap integral called the *formation amplitude*, f_{kl_k}, given by,

$$f_{kl_k}(r') = \int dx_D dx_\alpha d\vec{r} \mathcal{A}_{D\alpha} \left[\frac{\delta(r-r')}{r^2} \Psi_{kl_k}^{(D\alpha)}(x_D x_\alpha \hat{r}) \right]^* \Psi_{IM}^{(M)}(X_M). \tag{3.34}$$

Inserting the formation amplitudes in the current expression (3.20) gives the α-decay width,

$$\Gamma = \sum_{kl_k} \Gamma_{kl_k}, \tag{3.35}$$

where Γ_{kl_k} is the partial width for channel kl_k,

$$\Gamma_{kl_k} = \frac{\hbar^2 \kappa}{\mu} \frac{|r_V f_{kl_k}(r_V)|^2}{|H_{l_k}^{(+)}(\eta, \kappa r_V)|^2}, \tag{3.36}$$

where the outgoing Coulomb wave function $H_{l_k}^{(+)}$ is evaluated for the channel energy Q_k. The product appearing in the partial width (3.36), is often grouped in two factors: the *reduced width*,

$$\gamma_{kl_k}^2(r_V) = \frac{\hbar^2}{2\mu r_V} |r_V f_{kl_k}(r_V)|^2, \tag{3.37}$$

which has the unit of energy (e.g. MeV), and the unit-less *Coulomb penetrability*,

$$P_{l_k}(Q_k, r_V) = \frac{\kappa r_V}{|H_{l_k}^{(+)}(\eta, \kappa r_V)|^2}, \tag{3.38}$$

leading to the following expression for the partial decay width,

$$\Gamma_{kl_k} = 2\gamma_{kl_k}^2(r_V) P_{l_k}(Q_k, r_V). \tag{3.39}$$

The reduced width $\gamma_{kl_k}^2(r_V)$ contains all the effects of nuclear structure through the formation amplitude, whereas the penetrability $P_{l_k}(Q_k, r_V)$ is a strongly energy dependent factor describing the tunneling probability of structureless particles. In this work, the penetrability is calculated using the Coulomb wave function code of N. Michel [65]. Due to the very strong energy dependence of this factor, the experimental Q_k values are used when available. The calculation of the formation amplitudes is discussed in the next section.

3.2 Calculation of formation amplitudes

In this thesis α-decay is modeled using HFB wave functions for the mother and daughter states. To use the HFB wave functions described in chapter 2 the two following approximations are needed:

Pseudo-bound states: The HFB states are approximate bound-state eigenfunctions, that implies they do not satisfy the outgoing boundary condition in the α-daughter channels (3.25), assumed for the Gamow state. On the other hand, the α-decay widths Γ are so small that one can neglect the complex energy in the wave function up to α-daughter separations r well into the Coulomb barrier. Furthermore, due to the large barrier, the normalization of a bound state wave function will be very similar to the normalization employed in the current expression, c.f. Eq. (3.16), when r_V is in the Coulomb barrier.

Heavy-core approximation: The description in Section 3.1.3 employs internal coordinates for the mother and daughter nuclei, where the center of mass coordinate is not included. Use of such Jacobi coordinates for large systems becomes technically very challenging due to antisymmetrization. The HFB wave functions are defined in an oscillator basis and thus includes a redundant center of mass coordinate.

To proceed we consider the mother and daughter nuclei fixed at the origin. The vector between the daughter and α particle, $\vec{r}$, is approximated by the vector between the origin and the α-particle center of mass, and the internal coordinates of the daughter nucleus x_D is taken to include its center of mass. The formation amplitude in this approximation is compared to the amplitude when using intrinsic wave functions in Ref. [66]. The heavy-core approximation underestimates the formation amplitude slightly, with the error decreasing when the ratio $4/A_D$ between the α-particle and daughter nucleus masses becomes smaller.

The coordinate system used is the "lab" coordinates for $A_D + 4$ particles with coordinate $i = 1, 2$ referring to protons, and $i = 3, 4$ to neutrons in the α cluster. The internal coordinates of the α cluster, x_α, are the spins s_i and the Jacobi coordinates $\vec{r}_\pi, \vec{r}_\nu, \vec{r}_\alpha, \vec{R}_\alpha$, related to lab coordinates through,

$$\begin{pmatrix} \vec{r}_\pi \\ \vec{r}_\nu \\ \vec{r}_\alpha \\ \vec{R}_\alpha \end{pmatrix} = \frac{1}{2} \begin{pmatrix} \sqrt{2} & -\sqrt{2} & 0 & 0 \\ 0 & 0 & \sqrt{2} & -\sqrt{2} \\ 1 & 1 & -1 & -1 \\ 1 & 1 & 1 & 1 \end{pmatrix} \begin{pmatrix} \vec{r}_1 \\ \vec{r}_2 \\ \vec{r}_3 \\ \vec{r}_4 \end{pmatrix} . \tag{3.40}$$

For a daughter nucleus with A_D particles the employed internal coordinates are

$$x_D = \{x_5, x_6, \ldots, x_{Z_D+4}; x_{Z_D+5}, \ldots, x_{A_D+4}\} , \tag{3.41}$$

where x_i refers to the lab coordinate and spin of particle i, with $5 \leq i \leq Z_D + 4$ referring to protons and the rest to neutrons. The coordinates x_α, Eq. (3.40), are chosen to make

transformations of harmonic-oscillator wave functions more symmetric. The functional determinant of the transformation (3.40) has modulus 1, so the lab integration measure is preserved:

$$d\vec{r}_1 d\vec{r}_2 d\vec{r}_3 d\vec{r}_4 = d\vec{R}_\alpha d\vec{r}_\alpha d\vec{r}_\pi d\vec{r}_\nu \tag{3.42}$$

The vector $\vec{R}_\alpha$ is twice the physical center of mass vector $\vec{r}$,

$$\vec{R}_\alpha = 2\vec{r}. \tag{3.43}$$

Using the coordinate system (3.40), the formation amplitude $f_{kl_k}(r)$ can be expressed as,

$$f_{kl_k}(r) = \sqrt{8} g_{kl_k}(2r), \tag{3.44}$$

with the overlap integral g_{kl_k} defined below. The factor $\sqrt{8} = 2^{3/2}$ arises when comparing the normalization implied by the current expression, Eq. (3.33), to the lab-system normalization of the HFB wave function, and taking into account the relation (3.43). The overlap integral entering in Eq. (3.44) is defined,

$$g_{kl_k}(R'_\alpha) = \int dx_D dx_\alpha d\vec{R}_\alpha \mathcal{A}_{D\alpha} [\Psi_k^{(D)}(x_D), \Phi_{l_k}^{(c)}(R'_\alpha; x_\alpha, \vec{R}_\alpha)]^*_{IM} \Psi_{IM}^{(M)}(x_M), \tag{3.45}$$

where $\Psi_{IM}^{(M)}$ and $\Psi_k^{(D)}$ are the HFB wave functions for the mother and daughter. The localized cluster state $\Phi_{l_k m_{l_k}}^{(c)}$ is defined,

$$\Phi_{l_k m_{l_k}}^{(c)}(R'_\alpha; x_\alpha, \vec{R}_\alpha) = \Phi_{00}^{(\alpha)}(x_\alpha) \frac{\delta(R_\alpha - R'_\alpha)}{R_\alpha^2} Y_{l_k m_{l_k}}(\hat{R}_\alpha), \tag{3.46}$$

where $\Phi_{00}^{(\alpha)}(x_\alpha)$ is the intrinsic α-particle wave function. We employ the standard approximation for the α-particle wave function [56],

$$\begin{aligned} &\Phi_{00}^{(\alpha)}(\vec{r}_\pi, \vec{r}_\nu, \vec{r}_\alpha, s_1, s_2, s_3, s_4) \\ &= \left(\frac{4}{b_\alpha^3 \sqrt{\pi}}\right)^{3/2} e^{-\frac{r_\pi^2 + r_\nu^2 + r_\alpha^2}{2b_\alpha^2}} \left(\frac{1}{\sqrt{4\pi}}\right)^3 \\ &\times [\chi_{\frac{1}{2}}(s_1), \chi_{\frac{1}{2}}(s_2)]_{00} [\chi_{\frac{1}{2}}(s_3), \chi_{\frac{1}{2}}(s_4)]_{00}, \end{aligned} \tag{3.47}$$

where $\chi_{\frac{1}{2} m_s}(s_i) = \delta_{m_s s_i}$ is a spin wave function. The commonly used value of the oscillator length $b_\alpha = 1.42$ fm [55], giving a reasonable approximation of the ^{4}He charge density, is employed in this work.

The localized cluster state (3.46) can be expanded in a basis,

$$|\Phi_{l_k m_{l_k}}^{(c)}(R'_\alpha)\rangle = \sum_{i<j} \sum_{k<l} |ijkl\rangle \langle ijkl| \Phi_{l_k m_{l_k}}^{(c)}(R'_\alpha)\rangle, \tag{3.48}$$

where $|ijkl\rangle = a^\dagger_{\pi i} a^\dagger_{\pi j} a^\dagger_{\nu k} a^\dagger_{\nu l} |0\rangle$ and the overlaps appearing in the sum are given by,

$$\langle ijkl | \Phi^{(c)}_{l_k m_{l_k}}(R'_\alpha)\rangle = \int d\vec{R}_\alpha dx_\alpha \phi^*_{ij}(x_1 x_2)\phi^*_{kl}(x_3 x_4)\Phi^{(c)}_{l_k m_{l_k}}(R'_\alpha; x_\alpha, \vec{R}_\alpha), \tag{3.49}$$

with the two-particle wave functions,

$$\phi_{ij}(x_1 x_2) = \frac{1}{\sqrt{2}}\left(\phi_i(x_1)\phi_j(x_2) - \phi_i(x_2)\phi_j(x_1)\right). \tag{3.50}$$

Inserting the expansion (3.48) into (3.45), we get,

$$\begin{aligned} g_{kl_k}(R'_\alpha) = \frac{1}{2}\sum_{M_D m_{l_k}} C^{I_M M_M}_{I_D M_D l_k m_{l_k}} \sum_{ij}\sum_{kl} \langle D; k | a_{\nu l} a_{\nu k} a_{\pi j} a_{\pi i} | M; I_M M_M\rangle \\ \times \int d\vec{R}_\alpha dx_\alpha \Phi^{(c)*}_{l_k m_{l_k}}(R'_\alpha; x_\alpha, \vec{R}_\alpha)\phi_i(x_1)\phi_j(x_2)\phi_k(x_3)\phi_l(x_4), \end{aligned} \tag{3.51}$$

where $\langle D; k | a_{\nu l} a_{\nu k} a_{\pi j} a_{\pi i} | M; I_M M_M\rangle$ is a four-particle transfer amplitude.

The overlap integral, Eq. (3.51), is evaluated by using the spherical harmonic oscillator (SHO) basis. For each combination of four oscillator basis states *ijkl*, the overlap integral $I_{ijkl}(R'_\alpha)$,

$$I_{ijkl}(R'_\alpha) = \int d\vec{R}_\alpha dx_\alpha \Phi^{(c)*}_{l_k m_{l_k}}(R'_\alpha; x_\alpha, \vec{R}_\alpha)\phi_i(x_1)\phi_j(x_2)\phi_k(x_3)\phi_l(x_4), \tag{3.52}$$

is evaluated by transforming the product of the four oscillator wave functions to the coordinate system (3.40) using Talmi-Moshinsky brackets [67]. This transformation turns the integral $I_{ijkl}(R'_\alpha)$ into sums over products of one-dimensional integrals weighted by transformations coefficients. Many of the factors appearing are common for different combinations of oscillator indexes *ijkl*, and can be pre-calculated and stored allowing for an efficient numerical evaluation. This is used in the code presented in the Appendix.

The formula (3.51) is quite general and is valid for general mother and daughter many-body wave functions defined in the lab system and having good spin quantum numbers. These wave functions enter through the four-particle transfer amplitudes $\langle D; k | a_{\nu l} a_{\nu k} a_{\pi j} a_{\pi i} | M; I_M M_M\rangle$.

3.2.1 Pauli effects

The formation amplitude defined in Sections 3.1.3 and 3.2 should be used only when the distance r between the α cluster and daughter nucleus is large enough so that they do not have appreciable spacial overlap. This formation amplitude obeys the Pauli principle through the anti-symmetrization $\mathcal{A}_{D\alpha}$ in Eq. (3.45). The Pauli principle translates to the

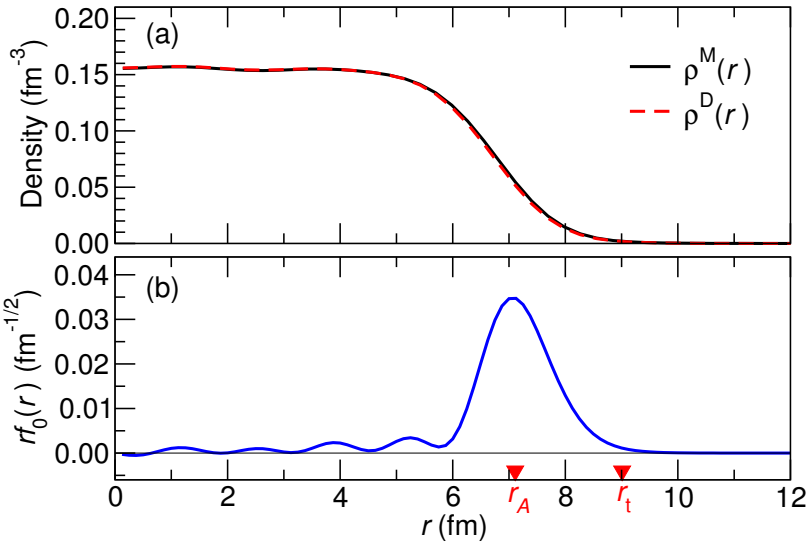

Figure 3.2: Ground-state-to-ground-state α-decay of ^{212}Po described using HFB wave functions obtained with the Skyrme interaction SLy4 [69] and the ``mixed pairing'' of paper III. (a) Local density $\rho_0^{M(D)}(r)$ for the mother(daughter) nucleus. (b) The formation amplitude $f_0(r)$, Eq. (3.44), multiplied by r. The red triangles show $r_A = 1.2$ fm $\times$ $208^{1/3} = 7.1$ fm, the standard nuclear radius for the daughter, and the touching radius $r_t = 9.0$ fm, Eq. (3.53).

fermion commutation relations for the annihilation operators in the four-particle transfer amplitudes.

When the α particle and daughter have spacial overlap, the wave function,

$$\mathcal{A}_{D\alpha}[\Psi_k^{(D)}(x_D), \Phi_{l_k}^{(c)}(R'_\alpha; x_\alpha, \vec{R}_\alpha)]^*_{IM},$$

appearing in the overlap (3.45) is not normalized in the cluster-angular coordinates $x_D x_\alpha \hat{r}$. The localized cluster state $\Phi_{l_k}^{(c)}$ will then have components corresponding to Pauli-blocked orbitals in $\Psi_k^{(D)}$, and the norm will be smaller than 1, c.f. the discussion in Ref. [68]. This suppresses the formation amplitude (3.34) in the interior of the daughter nucleus, giving rise to a surface-peaked function $f_{kl_k}(r)$, see Fig. 3.2.

This suppression can be corrected for by using the modified formation amplitude introduced by Fliessbach [68, 70], and discussed in the review [55]. The modified formation amplitude becomes much larger in the nuclear interior and reduces to the formation amplitude employed in this thesis when r becomes large. The modified formation amplitude has a more clear interpretation as a clustering amplitude in the nuclear interior, and can be used to define an α-cluster spectroscopic factor. To obtain the modified formation amplitude requires the calculation of norm-kernels, which was done in e.g. Refs. [66, 71].

To obtain the decay rate, the α-daughter potential is needed. At small radii r the strong-force contributions become important, whereas for larger r only the well-known Coulomb

interaction is needed. If the mother and daughter wave functions are well described to large radii, the complications associated with calculating the modified formation amplitude and the uncertainty of the strong-force α-daughter interaction can be avoided. The cost is that a large oscillator basis has to be used in the calculations to obtain a converged formation amplitude at large separations r. In the calculations presented in papers I-III the decay width is evaluated at the touching radius,

$$r_t = r_0(4^{1/3} + A_D^{1/3}), \tag{3.53}$$

where $r_0 = 1.2$ fm. The convergence of the formation amplitude with respect to the size of the oscillator basis is investigated in papers I and II. At least 15 major oscillator shells should be used for the mother and daughter HFB wave functions; in the papers I-III, 30 major oscillator shells are used.

3.2.2 Two-particle transfer amplitudes

In this work proton-neutron mixing is not considered so the four-particle transfer amplitudes in Eq. (3.51) factorize into a product of two two-particle transfer densities,

$$X_{ij}^{k(q)} = \langle D^{(q)}; k | a_j a_i | M^{(q)}; I_M M_M \rangle, \tag{3.54}$$

where $q = \mathrm{n(p)}$ indicates the neutron(proton) part. In papers I and II, ground-state-to-ground-state α-decays of even-even near-spherical nuclei are considered. The states eneter-ing in Eq. (3.54) are then,

$$|M; I_M M_M\rangle = |M_{00}\rangle, \tag{3.55}$$

and

$$|D; k\rangle = |D_{00}\rangle, \tag{3.56}$$

where $|M(D)_{00}\rangle$ is the spin $I = 0$ HFB vacuum for the mother(daughter) nucleus, see Sec. 2.2.1). Both states are represented in the same SHO basis trough their respective HFB U and V matrices, cf. Eq. (2.1).

For paper III, α-decay of odd-A near spherical nuclei are considered. The mother and daughter states are approximated by one-quasiparticle states, discussed in Sec. 2.2.3. For a fixed mother nucleus state a with spin I_M and projection M_M, the states considered can be written,

$$|M; I_M M_M\rangle = \beta^{(M)\dagger}_{aI_M M_M} |M_{00}\rangle, \tag{3.57}$$

and

$$|D; k\rangle = \beta^{(D)\dagger}_{k} |D_{00}\rangle. \tag{3.58}$$

Here $|M(D)_{00}\rangle$ is the spin $I = 0$ HFB vacuum of an even-even nucleus with average particle numbers corresponding to the studied odd-A nuclei. The quasiparticle creation operators

$\beta^{(M)\dagger}$ and $\beta^{(D)\dagger}$ are defined with respect to their respective vacuums $|M_{00}\rangle$ and $|D_{00}\rangle$, i.e. the expansion (2.1) of these operators in terms of the SHO basis involve different U and V matrices.

As the mother and daughter HFB vacua generally have non-zero overlap, $\langle D_{00}|M_{00}\rangle \neq 0$, the Thouless theorem can be used to compute the required two-body transfer amplitudes (3.54). Expanding $|M_{00}\rangle$ in terms of $|D_{00}\rangle$ and using Wick's theorem, the transfer densities can be expressed in terms of the U and V matrices for the mother and daughter, $U^{(M)}$, $V^{(M)}$, $U^{(D)}$, $V^{(D)}$ [32]. This results in the expressions found in Appendix B of paper III. The formulas for the transfer densities involve the common factor $\langle D_{00}|M_{00}\rangle$. For the α-decay calculations in this thesis only the modulus squared of this factor $|\langle D_{00}|M_{00}\rangle|^2$ enter in the physical observables, so the Onishi formula [32] can be used.

3.3 Results

The description of α decay employs the well established SHFB model, outlined in Chap. 2. This model can be applied in the whole nuclear chart, and contains no free parameters tuned to α-decay rates. The explicit correlations in the SHFB wave functions are on the other hand quite simple, with only pairing between like nucleons included. As shown in e.g. Refs. [66, 71, 72], the formation amplitude is sensitive to nucleon correlations, and increases substantially when wave functions containing more correlations are used. The formation amplitude probes surface correlations of four nucleons, and to reproduce the absolute value of the experimental decay width Γ requires the explicit inclusion of correlations that are not included in the SHFB models. As shown in these studies the slope of the tail of the formation amplitude is also sensitive to correlations, moving towards the value implied by the experimental Q_α-value when the correlations increase.

By using a large spherical harmonic oscillator basis, it is shown in papers I and II that the SHFB formation amplitudes at the touching radius r_t are numerically stable with respect to the basis size. However, the slope of the tail of the formation amplitude turns out to be too steep, and the absolute values turn out too small when using the SHFB wave functions. The description of relative decay rates is on the other hand good.

3.3.1 Relative decay rates

The decay widths Γ, Eq. (3.35), are evaluated using experimental Q_α values when available and using the matching radius $r_V = r_t$, where r_t is the touching radius, Eq. (3.53). The method as implemented uses spherical SHFB wave functions, implying only near-spherical nuclei can be described. We limit the application to nuclei where the quadrupole deforma-

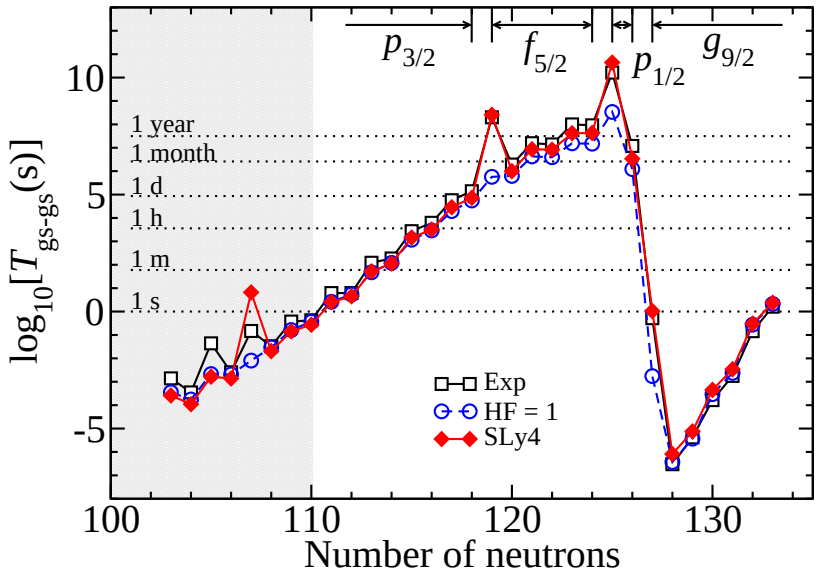

Figure 3.3: Figure from paper III. Ground-state-to-ground-state partial α-decay half lives for Po isotopes. The shaded area shows where the mother or daughter nuclei can no longer be considered near-spherical $|\beta_2| > 0.1$. The blue circles show the half-life only taking into account the s-wave Coulomb penetrability, with the reduced width $\gamma^2_{\ell 0}(r_t)$, Eq. (3.37), set to an average value for even nuclei. The red diamonds show results of the microscopic calculations, for calculation details see paper III.

tion parameter β_2 is small, $|\beta_2| < 0.1$.

Figure 3.3 shows the quality of the description of relative α-decay rates for Po isotopes. The theoretical ground-state-to-ground-state (gs-to-gs) partial half lives shown are defined,

$$T_{\text{gs-gs}} = \frac{\hbar \ln(2)}{\mathcal{S} \sum_{l_k} \Gamma_{kl_k}}, \tag{3.59}$$

where k labels the daughter nucleus gs configuration, and the sum is over all partial waves l_k allowed by angular momentum and parity conservation. The decay widths for all cases are multiplied by a same phenomenological factor $\mathcal{S}$. This single free parameter $\mathcal{S}$ is determined so that the gs-gs reduced widths, Eq. (3.37), for all the near-spherical even-even nuclei studied in paper I, are on average equal to the corresponding quantities extracted from experimental data. The results in Fig. 3.3 show the strong dependence of the half life on the Q_α value, which starts around 8.0 MeV for the lightest isotopes and decreases rather smoothly until the $N = 126$ gap is crossed, where Q_α jumps to a higher value before it decreases again. The microscopic results also capture the fluctuations in the half-life rel-

ative to the purely energy dependent barrier penetration (blue circles). The most striking fluctuations are associated with the hindered decays when the odd particle changes orbital.

The reduced width in Eq. (3.37) is valid for a given partial wave l_k. For decay of odd-A nuclei several partial waves contribute. To study the overall structure dependence of the decay rate an equivalent s-wave reduced width $\bar{\gamma}_k^2$ can be defined,

$$\bar{\gamma}_k^2 = \frac{\mathcal{S} \sum_{l_k} \Gamma_{kl_k}}{2P_0(Q_k^{\text{exp}}, r_t)}, \tag{3.60}$$

where k indicates that the partial decay widths Γ_{kl_k} are for a given mother nucleus state to a given daughter nucleus state. P_0 is the s-wave Coulomb penetrability, Eq. (3.38), and Q_k^{exp} is the measured Q value for this decay. From the experimental partial decay rate $\lambda_k = I_k \ln(2)/T$, where T is the measured half-life and I_k is the branching ratio for the particular decay, a corresponding experimental equivalent reduced width can be obtained,

$$\bar{\gamma}_{\text{exp},k}^2 = \frac{\hbar \lambda_k}{2P_0(Q_k^{\text{exp}}, r_t)}. \tag{3.61}$$

These reduced widths give a measure of the hindrance of different α-decay channels; by comparing with an average value for even-even nuclei $\langle \bar{\gamma}^2 \rangle$, a smaller $\bar{\gamma}^2$ indicates a hindrance due to nuclear structure. The reduced widths extracted from experiment (3.61) and results from microscopic calculations (3.60) are compared in Fig. 3.4.

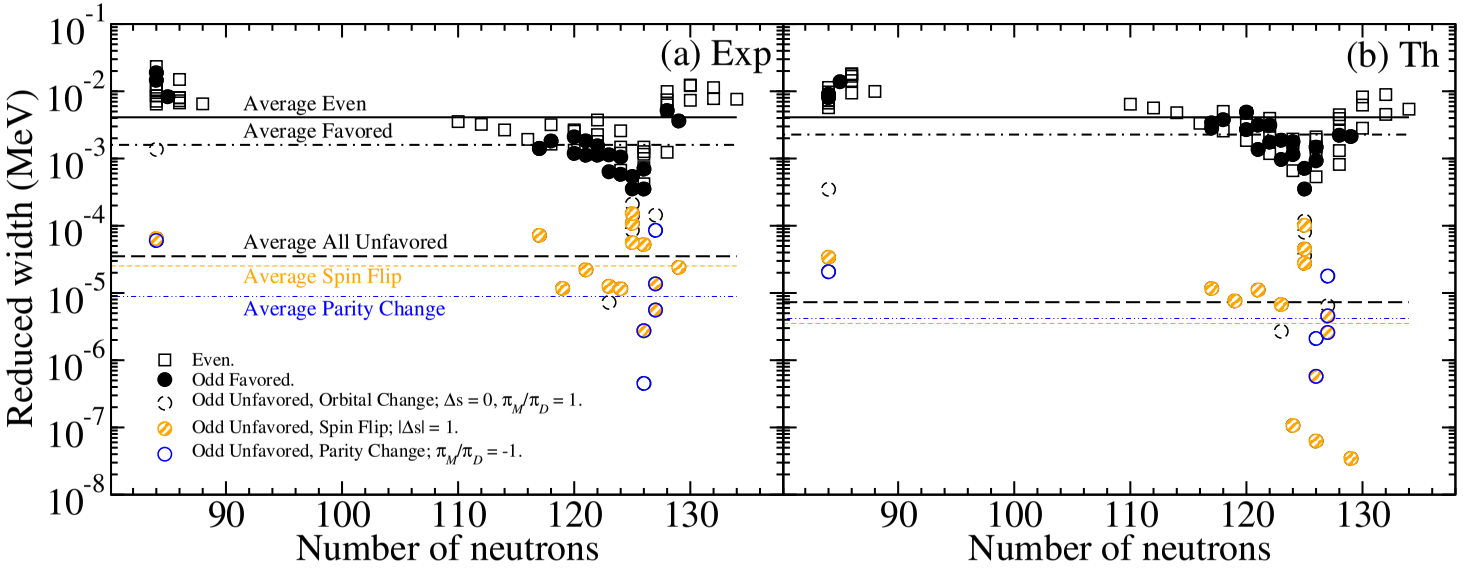

Figure 3.4: Figure from paper III. Reduced widths for α-decays of near-spherical even-even and odd-A nuclei. The odd-nucleus decays are grouped according to how the odd particle orbital changes. (a) Extracted from experimental partial half-lives using Eq. (3.61). (b) Theoretical results, Eq. (3.60).

α-decay of near-spherical even-even and odd-A nuclei where the spin and parity of the mother and daughter states are well known are considered in the study. All cases where the mother and daughter states can be interpreted as zero or one-quasiparticle states are included (excluding cases involving states interpreted as having a large vibrational component). For the odd-A cases shown, several data points can belong to different decay paths of the same mother nucleus. Resolved case-by-case most of the theoretical data points lie within a factor of 3 from experiment, see Fig 1 in paper III.

The odd-A cases are labeled according to how the orbital of the odd particle changes in the decay. The horizontal lines show the geometrical average of the reduced width for a given group of decays. From the fluctuation around the average values within the different groups, exhibited by the experimental data and fairly well reproduced by the microscopic calculations, one can conclude that the hindrance of a given decay channel is sensitive to the details of the nuclear wave functions. To describe the competition between different α-decay paths for the mother nucleus, approximate selection rules for the hindrance factor, e.g. those in Ref. [13] or using the average horizontal lines, can give only a rough approximation to the hindrance. To describe the competition in detail, microscopic calculations should be carried out.

3.3.2 α decay to excited states in superheavy nuclei

As mentioned in Chapter 1 superheavy nuclei (SHN) formed in heavy-ion fusion reactions often decay through a chain of α decays. In odd nuclei the gs-gs α decay can be significantly hindered when the odd nucleons occupy different orbitals in the mother and daughter. The previous section contained some examples of this for odd-A nuclei. If the gs-gs decay is sufficiently suppressed compared to the favored decay, where the odd particle remains in the same orbital, the favored α-decay path can dominate although its Q_α value is smaller. The daughter nucleus then ends up in an excited state after the α decay. This state can subsequently decay electromagnetically, e.g. by γ-emission or internal conversion. By measuring this subsequent decay in an α-γ spectroscopy experiment, one can obtain detailed nuclear-structure information for the superheavy daughter nucleus [11, 21].

Predicting for which nuclei α-decay to excited states takes place provides and important guide to experiment. Figure 3.5 shows calculated Q_α values for gs-gs decays (solid lines) and for favored decays when the excitation energy of the favored state is below 0.5 MeV (dashed lines). The locations where the dashed lines deviate from the solid lines indicate good candidates where one might observe α decay followed by γ emission. The available experimental data (solid circles) show that the Q_α values and excitation energies are reasonably well described by the present theory in the region of lower neutron numbers. Favored decays to excited states have been observed (open circles) at the locations suggested by the calculations in many cases.

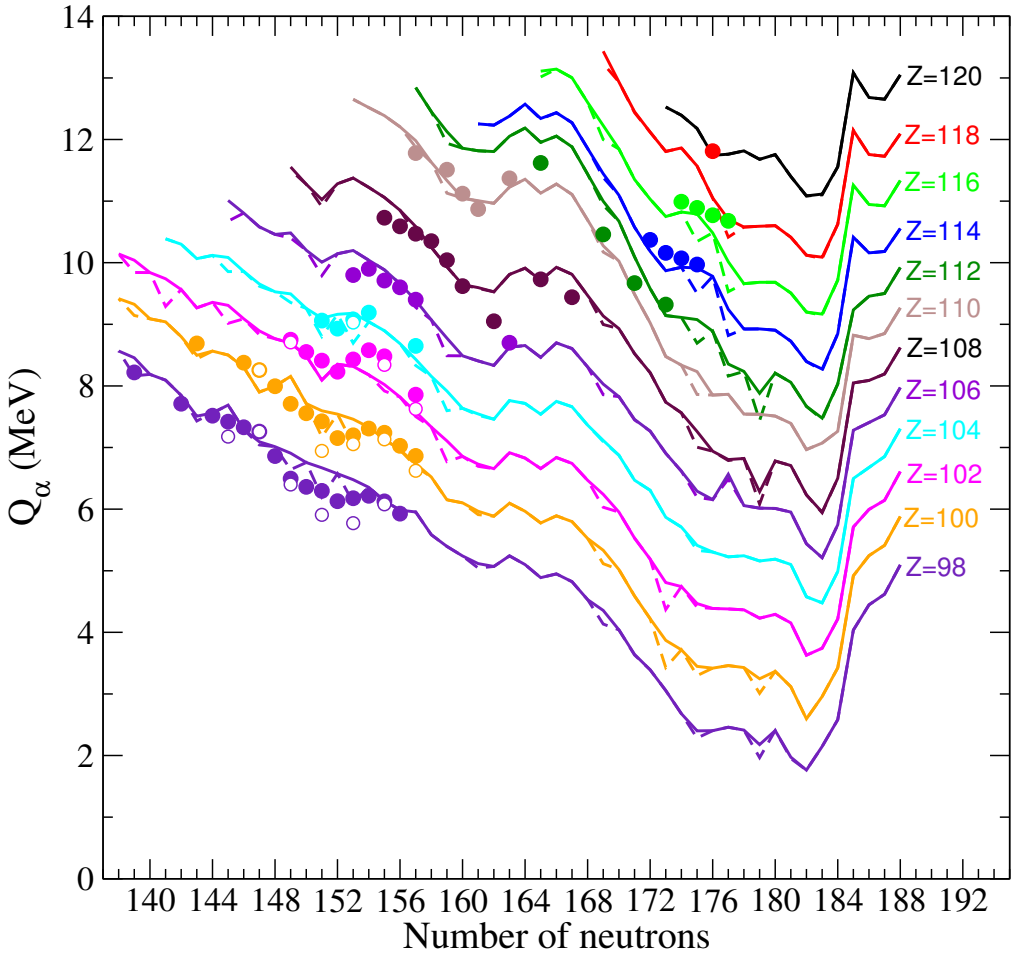

Figure 3.5: Figure from Ref. [73], Q_α values for heavy and superheavy nuclei. The lines show results from SHFB calculations allowing for axial deformations performed with the code of Ref. [74]. The Skyrme parametrization SLy4 and the ``mixed pairing'' of paper III is used. Solid lines -- gs-gs Q_α values, dashed lines -- Q_α values for favored decays. The circles show experimental data from Refs. [75, 76], solid circles -- gs-gs values, open circles -- favored decays.

The microscopic calculation of α-decay of deformed nuclei is beyond the present application of the method presented in this thesis. For the spherical SHN in figure 3.5, calculations can be carried out. The gs-gs partial half lives for even-even and odd-N nuclei are shown in Fig. 3.6. The gs-gs decays are hindered for $N = 179, 183,$ and 185, due to different orbitals for the odd neutrons in the mother and daughter nucleus ground states, for details see paper III.

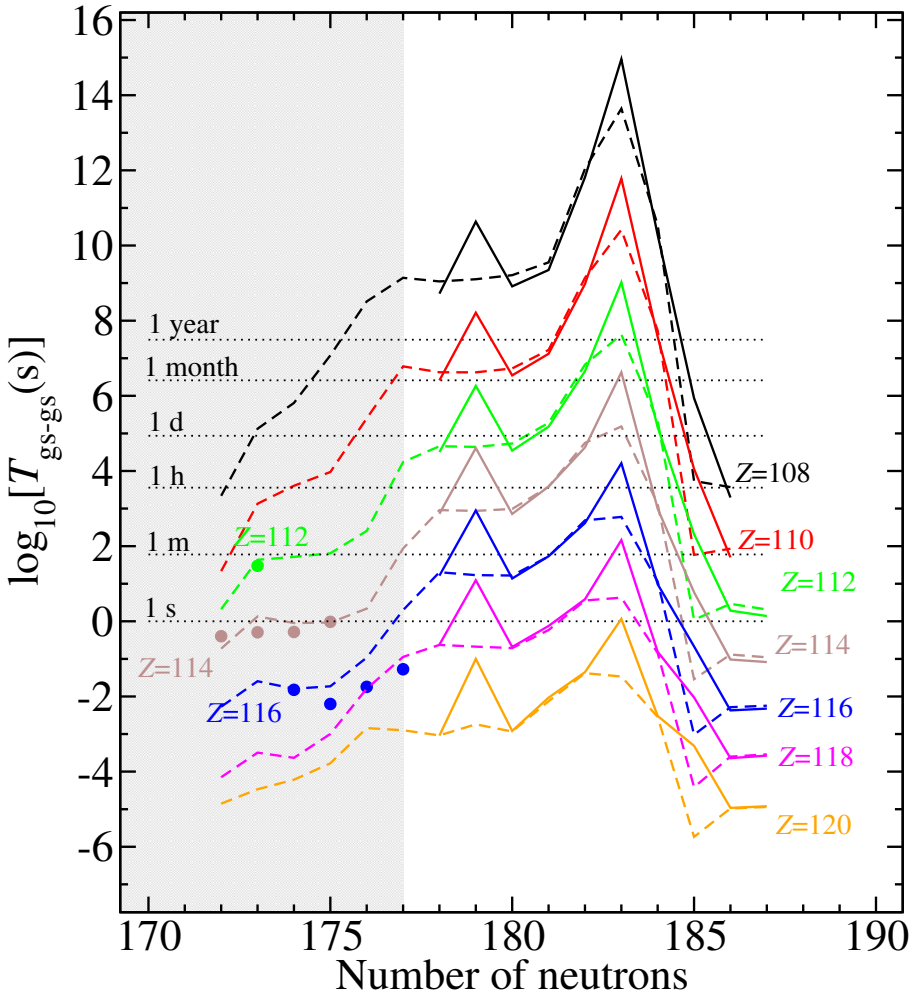

Figure 3.6: Figure from paper III, gs-gs partial half lives for superheavy nuclei. The lines show results of calculations using the gs-gs Q_α values in Fig. 3.5. Solid lines -- microscopic calculation. Dahsed lines -- calculation not taking into account variations in nuclear structure, obtained in the same way as the open circles in Fig. 3.3. Circles -- experimental data [75].

3.4 Outlook

The spherical HFB approach provides a good staring point for considering more involved nuclear wave functions. One possible extension is to consider α-decay of deformed nuclei. The next PhD student in the Lund nuclear theory group, M. Albertsson, has already started work in this direction.

The calculation of formation amplitudes using Eq. (3.51), makes the use of four-particle transfer amplitudes obtained from other types of wave functions straightforward. An inter-

esting prospect is to study α-clustering effects of beyond-mean-field correlations contained in wave functions of *ab-inito* nuclear structure models.

If additional correlations can be included in a way that is not too numerically costly, one could consider to include the open-channel α-decay boundary condition in the nuclear-structure calculation. This could be done in an approximate way by introducing a constraint on the slope of the formation amplitude $f(r)$. This type of boundary condition, fixing the asymptotics in the decay channel to those implied by the Q value, is employed in some quantum-monte-carlo calculations for light nuclei, see e.g. [77], and would remove any dependence on the matching radius r_V.

Chapter 4

Nuclear states in superheavy elements

Shell structure plays a very important role for the stability of superheavy elements [4]. Without quantum-mechanical shell effects, superheavy nuclei (SHN) would spontaneously fission with a very short lifetime. Predictions for the location in the nuclear chart of the most stable SHN are strongly dependent on the shell structure obtained in the nuclear-structure models. The shell structure also plays a large role in the low-energy excitation spectra of odd-A and odd-odd nuclei, providing a link between the shell gaps stabilizing SHN and the spectra.

The description of the low-energy spectra of deformed nuclei in the No-region ($Z = 102$) with SHFB models was investigated by Yue Shi and coworkers in Jyväskylä [78]. Nuclei in this region are the heaviest where good spectroscopic data is currently available. Similar to many commonly employed Skyrme parameterizations, the modern SHFB parameterization UNEDF1 [79] employed in that study provides a good description of bulk properties across the nuclear chart, but cannot describe spectra with the high accuracy required to reproduce experimental data. By tuning the spin-orbit and pairing properties locally in this region, the description of the low-energy spectrum could be improved. In deformed nuclei, single-particle states linked to high-lying spherical shells can show up as intruder states. Improving the description of these intruder states might then also improve the predictions for SHN.

The first direct experimental spectroscopic information for SHN is provided by the experiment on element 115 [21] lead by the Lund experimental nuclear structure group. Paper IV in this thesis is a collaboration between the Jyväskylä group and Lund investigating the structure of nuclei produced in the α-decay chains of $^{288}115_{173}$.

In this paper the tuned UNEDF1 parameterization, UNEDF1$^{\mathrm{SO}}$, is tested against the experimental data. An alternative to the SHFB and similar self-consistent mean field models is the Macroscopic-Microscopic (MM) models. Using parameters tuned for actinide nuclei

[80], the Nilsson-Strutinsky MM model is expected to provide reasonable predictions for SHN, which are compared with the experimental data and the predictions of the SHFB model. To describe the spectra in the odd-odd SHN studied in the experiment, the Nilsson-model single-particle wave functions are used in the particles+rotor model of Ref. [81].

4.1 Macroscopic-Microscopic models

The Macroscopic-Microscopic model is based on a division of the binding energy E into a macroscopic part E_{mac} and a microscopic part E_{mic}:

$$E(N, Z, \text{shape}) = E_{\mathrm{mac}}(N, Z, \text{shape}) + E_{\mathrm{mic}}(N, Z, \text{shape}). \tag{4.1}$$

The macroscopic part accounts for most of the binding energy, and describes the smooth variations in energy when N, Z, and the nuclear shape are varied. E_{mac} can be obtained from a Liquid-drop model of the nucleus, e.g. [28], or similar models such as the finite-range droplet model [29]. These models share many features with the early semi-empirical mass formulas such as that of von Weizsäcker [82].

The microscopic part accounts for the fluctuation of the energy around the smooth trends, due to the shell structure. E_{mic} consists of the shell-correction energy δE_{sh} and the pairing-correction energy δE_{pc}. δE_{sh} can be extracted using the Strutinsky approach [83, 84], which employs the single-particle energies from a phenomenological mean-field potential. Several different parameterizations of the mean-field can be used, e.g. the Nilsson Modified oscillator [8], the Woods-Saxon potential [85], or the Folded-Yukawa potential [29]. The shell correction captures the fluctuations in energy when filling single-particle levels in the mean-field potential, relative to the filling of particles in a smooth distribution of levels [86]. The pairing-correction energy is typically calculated using the BCS approach, which can be regarded as a simplified version of the HFB approach. In a similar way as the shell-correction energy, δE_{pc} is defined as a difference between the pairing correlations obtained with the mean-field level structure compared with a smooth level structure.

4.2 Particles + rotor model

In the particles-plus-rotor model, a deformed nucleus is described by dividing the system into a few valence particles and rotor, which models the collective rotation of the remaining particles. The rotor allows for an efficient description of the rotational bands in the spectrum. By coupling the single-particle orbitals of the deformed mean field, where the rotational symmetry is broken, to the phenomenological rotor wave function, states with good total angular momentum I are obtained.

The Hamiltonian employed in the model is,

$$H = H_{\text{val}} + H_{\text{coll}}, \tag{4.2}$$

where H_{val} describes the valence particles in the intrinsic body-fixed system, and H_{coll} describes the rotational energy of the rotor. The valence particles are described using BCS quasiparticles, $\alpha_k^\dagger$, obtained from a phenomenological mean-field single-particle Hamiltonian and a residual pairing interaction. The valence part of the Hamiltonian can be put in the form,

$$H_{\text{val}} = E_0 + \sum_k E_k \alpha_k^\dagger \alpha_k + V_{\text{pn}}, \tag{4.3}$$

where E_0 is the gs energy of the BCS vacuum, and E_k the quasiparticle energies. For odd-odd nuclei a proton-neutron interaction among the valence particles V_{pn} can also be included.

The rotor part is given by,

$$H_{\text{coll}} = \sum_{i=1}^{3} \frac{R_i^2}{2\mathcal{J}_i}, \tag{4.4}$$

where R_i is the projection of the rotor angular momentum $\vec{R}$ on body-fixed axis i, and $\mathcal{J}_i$ is the corresponding moment of inertia. The total angular angular momentum $\vec{I}$ is given by the sum of the angular momentum of the rotor $\vec{R}$ and of the valence particles $\vec{J}$,

$$\vec{I} = \vec{R} + \vec{J}. \tag{4.5}$$

The Hamiltonian (4.2) is diagonalized using the strong-coupling basis. The basis states $|\Psi^I_{MKn}\rangle$ are defined,

$$\begin{aligned} |\Psi^I_{MKn}\rangle &= \frac{1}{\sqrt{2}}(1 + \mathcal{R}_1)|IMK\rangle|n\rangle \\ &= \frac{1}{\sqrt{2}}\left(|IMK\rangle|n\rangle + (-1)^I|IM-K\rangle e^{-i\pi J_1/\hbar}|n\rangle\right), \end{aligned} \tag{4.6}$$

where $|IMK\rangle$ represents a normalized Wigner rotation matrix $\sqrt{\frac{2I+1}{8\pi^2}}\mathcal{D}^I_{MK}$. $|n\rangle$ represents a state of the intrinsic system, for the odd-odd nuclei a one-quasiproton-one-quasineutron state is used,

$$|n\rangle = \alpha^\dagger_{\pi_n}\alpha^\dagger_{\nu_n}|\text{BCS}\rangle. \tag{4.7}$$

For reflection symmetric deformations (no odd multipoles), the system is invariant to 180° rotations around the body-fixed axes. It is customary to symmetrize the basis state with respect to $\mathcal{R}_1 = e^{i\pi R_1/\hbar}$, a 180° rotation of the rotor around the body-fixed 1-axis [32].

Choosing the basis states to be symmetric eigenstates to the 180° rotations, $\mathcal{R}_i|\Psi^I_{MKn}\rangle = |\Psi^I_{MKn}\rangle$, for $i = 1, 2, 3$, ensures that the rotor describes an even-even rotating core [87]. In the case of no quasi-particles the symmetrization removes states with odd spins, implying the spin sequence $I = 0, 2, 4, \ldots$ characteristic of the ground-state (gs) band in even-even deformed nuclei.

4.2.1 Basic features of the particles-rotor spectrum

The particles+rotor model has been widely used, and is discussed in detail in many textbooks, e.g. [32, 88]. For the odd-odd SHN, we are interested in the low-energy states of the spectra, and we shall below discuss how H_{coll} affects the spectrum of the Hamiltonian (4.2).

The considered nuclei are predicted to be axially symmetric, which simplifies the calculations somewhat. Choosing the 3-axis as symmetry axis implies $\mathcal{J}_1 = \mathcal{J}_2 = \mathcal{J}$, and $R_3 = 0$. With Eq. (4.5), the rotor Hamiltonian (4.4) can then be written [32],

$$H_{\text{coll}} = H_{\text{rot}} + H_{\text{rec}} + H_{\text{cor}}, \tag{4.8}$$

where H_{rot} is the simple rotational-band contribution,

$$H_{\text{rot}} = \frac{1}{2\mathcal{J}}(I^2 - I_3^2). \tag{4.9}$$

H_{rot} does not mix the different basis states (4.6); it gives a diagonal contribution $\frac{1}{2\mathcal{J}}(I(I+1) - K^2)$, with the characteristic I-dependence of the energy for low-spin members of a rotational band. If the mixing introduced by the other terms are small, the dominating odd-odd band-head configuration $|n\rangle$ can be used to label rotational bands with $I = K, K+1, \ldots$. This is typically the case for well-deformed nuclei where the moment of inertia $\mathcal{J}$ is large. H_{rec} is the "recoil" term,

$$H_{\text{rec}} = \frac{1}{2\mathcal{J}}(J^2 - J_3^2). \tag{4.10}$$

Since it only depends on the valence-particle angular momentum $\vec{J}$ it acts only on the intrinsic part of the basis states (4.6). The most important effect of this term is to move the whole band up or down in energy. The size of this shift depends on the intrinsic band-head wave function [89]. H_{cor} is the "Coriolis" term,

$$H_{\text{cor}} = -\frac{1}{\mathcal{J}}(I_1 J_1 + I_2 J_2) = -\frac{1}{2\mathcal{J}}(I_+ J_- + I_- J_+). \tag{4.11}$$

This term couples the intrinsic system to the rotor, and causes a gradual alignment of the intrinsic spin $\vec{J}$ with the total angular momentum $\vec{I}$. It mixes states differing in K by one unit, $\Delta K = \pm 1$. For the odd-odd case the K values of the band-heads are integers, so there are no diagonal contributions from this term, and thus no decoupled $K = 1/2$ bands.

4.3 Element 115 decay chain

The decay chains of element 115 were studied in an experiment [21] lead by the Lund nuclear structure group, with measurements performed in 2012 at GSI Helmholtzzentrum für Schwerionenforschung, Darmstadt, Germany. The experiment was the first study using combined α-decay and γ/X-ray spectroscopy measurements to study the superheavy elements created in the ${}^{48}_{20}\mathrm{Ca}_{28}$ + ${}^{243}_{95}\mathrm{Am}_{148}$ reaction. Several α-decay chains assigned to ${}^{288}115_{173}$ were detected.

The ${}^{288}115_{173}$ chains consist of five α-decays ending in ${}^{268}_{105}\mathrm{Db}_{163}$, that decays by spontaneous fission. The spectra of these odd-odd nuclei are investigated using the two-quasiparticles+rotor model. The deformation parameters are obtained by minimizing the gs energy in the MM model employed in Ref. [90], using the Lublin-Strasbourg macroscopic energy [28], and the Modified-Oscillator (MO) potential, with parameters adjusted to actinide data from Ref. [80]. The particle-rotor model employed is that of Ref. [81], and the calculations are performed using the associated code written by I. Ragnarsson and P. B. Semmes.

Since there is no well-established proton-neutron residual interaction applicable to this region, the calculations are performed with $V_{\mathrm{pn}} = 0$. Studies of deformed odd-odd nuclei in the rare-earth region suggest that a finite-range effective interaction containing tensor terms should be used [91–93]. The most basic effect that should be modeled with the proton-neutron interaction is the Gallagher and Moszkowski rule [94]. For the two possible band-heads that are obtained by coupling the neutron(proton) quasiparticle angular-momentum projections $\Omega_{\nu(\pi)}$: $K_> = \Omega_\nu + \Omega_\pi$, and $K_< = |\Omega_\nu - \Omega_\pi|$, the one where the intrinsic spins are parallel is favored. The associated energy splittings introduced by V_{pn} are on the order of 100 keV in the rare-earth region [91]. A very rough estimation for the effects of the neglected residual proton-neutron interaction is thus shifts of bands relative to each other by similar amounts, $\sim$ 100 keV.

4.3.1 E1 transition and constraints on theory

In the detailed analysis of the experimental data it was found that the α-decay of ${}^{280}_{111}\mathrm{Rg}_{169}$ leaves the daughter nucleus ${}^{276}_{109}\mathrm{Mt}_{165}$ in an excited state, which then decays via $E1$ γ-decay [1, 21]. The $E1$ transition connects states with different parity, and difference in total angular momentum $\Delta I = 0, \pm 1$. For the body-fixed intrinsic system, these selection rules implies intrinsic configurations with different parity and with the projection of the angular-momentum on the symmetry axis, Ω, differing at most by one unit, $\Delta\Omega = 0, \pm 1$. The single-particle spectrum predicted with the MO allows for two single-quasiparticle transitions that fit these selection rules. The proton transition $\pi[615]11/2 \rightarrow \pi[505]9/2$, and

the neutron $\nu[716]13/2 \rightarrow \nu[606]11/2$. In the particle-rotor results, low-lying states involving these orbitals allow for either the proton or neutron $E1$ transition, both with roughly the same energy, 200 keV, as observed in experiment.

The particle+rotor calculations reveal the large amount of low-lying levels implied by both the many possible two-quasiparticle band heads and the rotational bands build upon these configurations, see Fig. 7 in paper IV. The details of the predicted spectrum is subject to quite large uncertainties. The energy order of the quasiparticle states is sensitive to details of the mean-field potential, that most likely involves errors due to the extrapolation to ^{276}Mt from the region where it was adjusted. The ordering of the band-heads is in turn sensitive to the recoil term in the rotor Hamiltonian, which is included in the calculations, and also to the proton-neutron interaction, which is not included. Due to the many close-lying levels, and the above mentioned uncertainties one cannot suggest a detailed decay scenario, such as spin or parity assignments of the states connected by the $E1$ transition.

The most robust constraint on theory is that of differing parity orbitals. Interestingly the SHFB parameterization, UNEDF1^{SO}, tuned to the No-region data does not allow for a simple explanation in terms of either neutron or proton single-quasiparticle transitions. It should be noted that configuration mixing can produce low-lying states that can be connected by an $E1$, implying that the spectra predicted by the model cannot be completely ruled out. The unmodified UNEDF1 parameterization allows for the single-proton transition suggested by the MO, but not for the neutron transition. Due to the self-consistent nature of the SHFB approach, several parameters simultaneously influence the location of the shells. When more data become available one can ascertain if the adjustment of the UNEDF1 parameterization locally in the Nobelium region implied an "overfitting", causing bad extrapolation properties compared to the original parametrization.

Observation of $E1$ transitions in neighboring odd-A nuclei would help to clarify the situation, and place a stronger constraint on models. Experiments on odd-proton and odd-neutron decay chains could possibly place the $E1$ on either the proton or neutron side. For odd-A nuclei predictions of the low-energy spectrum become less complex, allowing for a more direct comparisons with predicted quasiparticle spectra. In this context an interesting future project would be to predict α-decay branching ratios for these odd-A nuclei. This will be possible when the α-decay approach described in chapter 3 is extended to deformed nuclei.

Chapter 5

Fission fragment yields

Fission in a heavy nucleus may be induced by neutron capture, where the new combined system is excited by several MeV. If the excitation energy is higher than the fission barrier the nucleus splits into two fragments in a dynamical process. Measuring the fragment masses from a large number of fission events reveals a distribution of the fission yield. For fission of actinides such as uranium and plutonium, the yield distribution has two peaks showing that the split where one of the fragments is heavier is the most common. When the energy of the incoming neutron is increased these peaks decrease while the number of events where the fragments have similar masses increases.

Shortly after the discovery of nuclear fission, Bohr and Wheeler [6] proposed a theoretical description in terms of the liquid-drop model. Using the concept of an energy surface depending on parameters describing the nuclear shape, the basic features of fission could be explained. The driving mechanism is the Coulomb repulsion between protons which competes against the short-range attractive nuclear interactions. In the liquid-drop model these counteracting effects give rise to a fission barrier in the potential energy as a function of the elongation shape parameter.

The elongation and other shape parameters are in a classical description collective degrees of freedom for the nucleus. In a quantum-mechanical mean-field description the shape is instead described by a symmetry-breaking local density $\rho(\vec{r})$. After the capture of the neutron the shape of the excited nucleus evolves with time to that of the separated fragments.

Important quantities to be described by a model for fission are the threshold energy for the reaction, the fragment mass distribution, what the excitation energies of the fragments are, and how many neutrons are released that can induce fission in other nuclei and drive a chain reaction. To describe in detail the mass and charge distribution of the fragments requires dynamical models for the shape evolution [95]. Different approaches to treat the

time-dependent dynamics employed in recent studies include the non-adiabatic energy-density-functional (EDF) [96], adiabatic-EDF [17], and the Langevin approach [97].

In paper V in this thesis, the energy dependence of the fission-fragment mass distribution is studied using the Brownian shape-motion (random walk) approach introduced by Randrup and Möller [22]. The random-walk approach offers an efficient method to calculate the fragment mass distribution, avoiding the complications of dealing with the time-dependence explicitly. It employs the macroscopic-microscopic mass model of Möller *et al.* [29], which has been very successful in describing ground-state masses. The mass model has been improved in several iterations [29, 98, 99] and applied successfully to other observables such as β-decay half-lives [100] and fission-barriers [101]. The description of asymmetric fission requires a flexible shape parametrization. Employing five independent shape parameters, calculations with the model reveal the complex topology of valleys and separating ridges in the potential energy landscape influencing the fission process [102].

The random-walk approach has proven to give a good description of observed fragment mass yields for many nuclei [23, 103, 104]. During the random walk the nuclear level density at different shapes plays a large role for the shape evolution. In the previous studies the level densities were included using a Fermi-gas expression, modified to approximately take into account the gradual damping of shell effects. The most recent prescription in Ref. [103] captures the overall trends in the energy dependence of the fission yields, but needed to be adjusted to data and does not include effects of the structure of the level density at lower energies. In paper V we explore the effect of the nuclear structure on the fission yields obtained when combining the Brownian shape-motion model with the microscopic level-density model of Ref. [24].

5.1 Random-walk model for fission yields

In the random-walk model the nuclear shape is described by five shape coordinates $\boldsymbol{\chi} = (\chi_1, \ldots, \chi_5)$. The shape space is discretized giving a lattice of over five million different shapes with potential energies $U(\boldsymbol{\chi})$ [101]. The shape evolution is assumed to be strongly damped so the collective kinetic energy is negligible. For a system with total energy E and total angular momentum I, all of the local excitation energy $E^*(\boldsymbol{\chi}) = E - U(\boldsymbol{\chi})$ is assumed to go to the intrinsic degrees of freedom described by the level density $\rho(I, E^*)$.

To obtain the yields a large number of random walks are performed. The steps in the random walk are determined by the Metropolis algorithm. From the current shape i a neighboring candidate shape j is selected at random. The probability $P_{i\to j}$ to accept a step is given by,

$$P_{i\to j} = \min\left[1, \rho_j(I, E^*(\boldsymbol{\chi}_j))/\rho_i(I, E^*(\boldsymbol{\chi}_i))\right], \tag{5.1}$$

where $\rho_{i(j)}(I, E^*)$ is the microscopic level density for the shape $i(j)$.

5.2 Nuclear level densities

The nuclear level densities are calculated using the combinatorial model of Ref. [24]. The level densities in the combinatorial model give a fair description of available experimental data. The previous application was to ground-state shapes, and we now apply the model to all shapes in the lattice. The method as implemented for this fission study takes into account rotation and pairing for each level, giving a micro-canonical description. For each shape, blocked BCS calculations are performed for each combination of particle-hole excitations in the Folded-Yukawa mean-field. The same mean-field is used to determine the shell and pairing correction energies that enters in the potential energy $U(\boldsymbol{\chi})$. The lowest potential-energy surface is obtained for even-even 0^+ configurations. In this section the energies E refer to the energy relative to this reference energy at the given shape $\boldsymbol{\chi}$.

All shapes considered have axial symmetry. Rotation is treated by considering the diagonal contribution from the collective rotation in the particles+rotor model, c.f. Sec. 4.2.1. This gives the rotational contribution E_{rot} to the energy,

$$E_{\text{rot}} = \frac{1}{2\mathcal{J}(\boldsymbol{\chi})}(I(I+1) - K^2). \tag{5.2}$$

Most of the five million shapes have considerable mass-asymmetry, and thus break the parity symmetry associated with invariance of the system to space inversions, described by the operator $\hat{\pi}$. In the level density calculations for paper V all shapes are treated in the same way, by considering the rotational bands suitable for large parity-breaking deformations [105]. The angular momentum I and parity π of the rotational band members built on the intrinsic multi-particle-multi-hole state $|i\rangle$ are given by,

$$I^\pi = \begin{cases} 0^+, 1^-, 2^+, 3^- \ldots & , \text{if } e^{-i\pi J_1}\hat{\pi}|i\rangle = |i\rangle \\ K^\pm, (K+1)^\pm, (K+2)^\pm \ldots & , \text{if } e^{-i\pi J_1}\hat{\pi}|i\rangle \neq |i\rangle \end{cases}, \tag{5.3}$$

where $e^{-i\pi J_1}$ comes from the symmetrization of the rotor $\mathcal{R}_1$ (c.f. Sec. 4.2), and $\hat{\pi}$ from the symmetrization of a degenerate asymmetric intrinsic state, c.f. Ref. [106]. Of the intrinsic states $|i\rangle$, only the seniority-zero states, where all quasiparticles are paired off in time-reversed orbitals are eigenstates to $e^{-i\pi J_1}\hat{\pi}$. The contribution to the level density from these states is small for all but the lowest energies [107].

The level density for a fixed angular momentum I is obtained by counting the states $E_k(I, \pi)$

in a bin of width ΔE centered around E_b, and averaging over parities,

$$\rho(I, E_b) = \frac{1}{2} \sum_{\pi} \frac{1}{\Delta E} \int_{E_b - \frac{\Delta E}{2}}^{E_b - \frac{\Delta E}{2}} \sum_{k} \delta \left(E - E_k(I, \pi) \right) dE. \tag{5.4}$$

For the mass-symmetric shapes a different rotational sequence, giving a level density with half the number of states [108], should in principle be used. The doubling of the level density associated with breaking the parity symmetry is instead taken into account approximately in the random walk. The lattice of shapes includes both of the asymmetric shapes that can be mapped onto each other by space inversion, effectively giving twice the level density for asymmetric shapes compared to symmetric shapes. When the mass asymmetry is non-zero, but not strongly symmetry breaking, mixing in this degree of freedom causes a splitting of parity doublets [105, 106, 109]. This should lead to a level density with values that are on the average in between those for symmetric and strongly asymmetric shapes. This gradual increase is neglected in the current approach.

5.3 Influence of nuclear structure on fission yield distributions

The potential energies $U(\boldsymbol{\chi})$ and the microscopic level densities $\rho(I, E^*(\boldsymbol{\chi}))$ at each shape are inputs to the fission calculations and enter at each step of the random walk through Eq. (5.1). The fragment charge yields for fission of ^{234}U obtained with the approach are shown in Fig. 5.1. Results obtained using the microscopic level densities are compared to the yields obtained using the previous prescription of Ref. [103], employing a Fermi-gas level density with a phenomenological damping function acting on the shell- and pairing-correction energies δE_{sh} and δE_{pc} (c.f. Sec. 4.1) that was adjusted to this case. The new calculations with the microscopic level densities reproduce the energy dependence of the yields well without any adjustable parameters.

Figure 5.2 shows the symmetric mass yield for the fission of the compound nucleus ^{236}U as a function of excitation energy. The yields resulting from calculations with the standard microscopic level densities reproduce the general increasing trend of the experimental data with increasing excitation, although the yield is slightly overestimated. The calculations show a non-monotonic increase of the symmetric yield with increasing energy. The bumps in the symmetric yield curve are sensitive to the pairing correlations. Increasing the pairing increases the size of the bumps and moves the second bump up in energy. Without pairing, the symmetric yield curve is smooth. Since the pairing is strongly damped with increasing excitation, it not immediately obvious that it should have an effect on the yields.

The structure of the symmetric yield as a function of energy resembles the low-energy structure of the microscopic level densities, c.f. Figs 1 and 13 in paper V. To fission symmetrically,

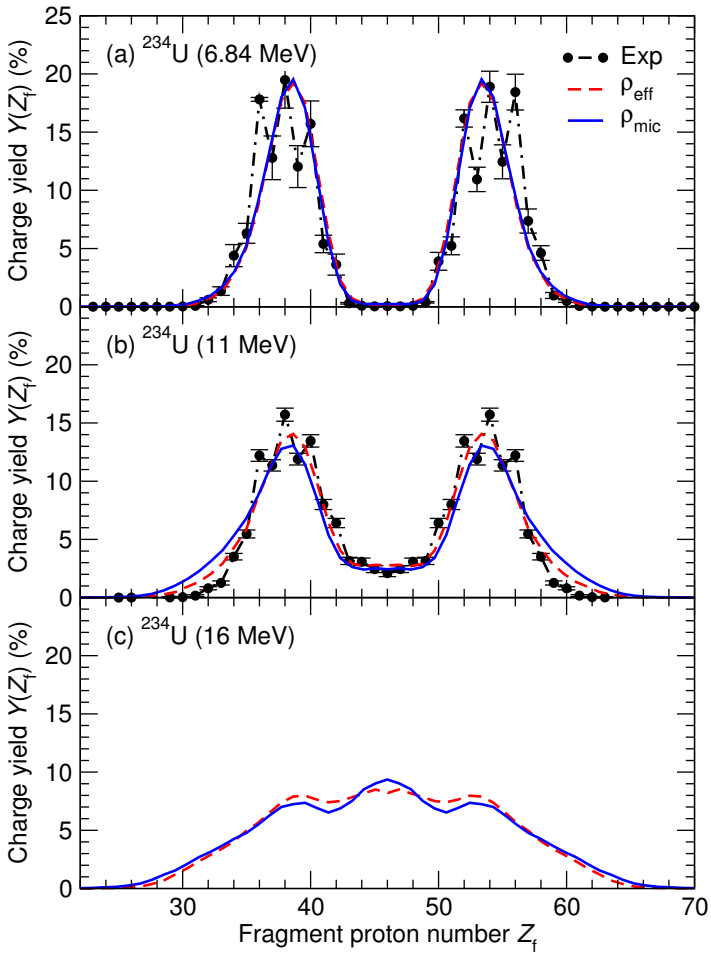

Figure 5.1: Figure from paper V. Fragment charge yields for fission of ^{234}U at different excitation energies. Blue solid lines: Results from calculations with microscopic level densities ρ_{mic}. Red dashed lines: calculations employing the previous prescription ρ_{eff} which was adjusted to reproduce the energy dependence of the experimental data (black dots). The new approach with ρ_{mic} reproduces the energy dependence without any adjustment to fission data.

the system has to cross a ridge separating the favorable asymmetric fission path from symmetric shapes (c.f. Figs 3 and 4 in paper V). At a ridge the local excitation energy E^* is several MeV smaller than for the second minimum and fission valleys, so the level density at low energies becomes important here. The single-particle level spacing is usually smaller at such ridges, giving a positive shell-correction energy and a large pairing-correlation energy. This results in level densities with pronounced bumps, similar to level densities shown by the blue curve in Fig. 1 and the curves in Fig. 13 in paper V.

The ridges are the lowest potential energy saddle points where random walks connecting the asymmetric fission path to the symmetric fission valley can pass. In general, there is not

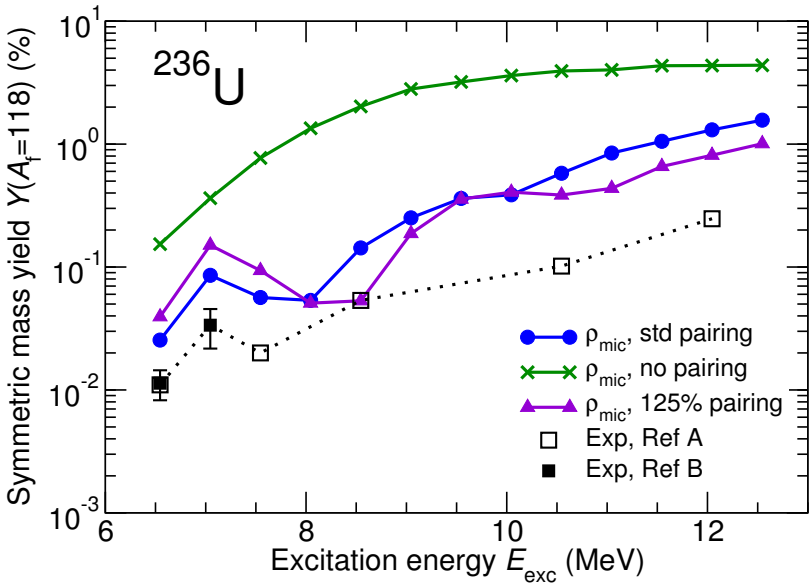

Figure 5.2: Figure from paper V. Symmetric mass yield for fission of ^{236}U as a function of excitation energy. The pairing properties of the microscopic level density influences the energy dependence of the calculated yields, giving rise to the structure shown by the blue and violet curves.

a single shape where all random walks giving symmetric fission must pass through. Still, a good starting point for constructing a simple explanation of the non-monotonic energy dependence in Fig. 5.2 is to consider only one point on the ridge. Consider the probability to go from a shape $\boldsymbol{\chi}_v$ in the asymmetric fission valley up to a ridge shape $\boldsymbol{\chi}_r$ in a fixed number of steps n,

$$P^{(n)}_{v\to r} \propto \rho_r(I, E^*(\boldsymbol{\chi}_r))/\rho_v(I, E^*(\boldsymbol{\chi}_v)), \tag{5.5}$$

where the local excitation energy $E^*(\boldsymbol{\chi}_v)$ is much larger than $E^*(\boldsymbol{\chi}_r)$ and thus the level density $\rho_v(I, E^*(\boldsymbol{\chi}_v))$ is much larger than $\rho_r(I, E^*(\boldsymbol{\chi}_r))$. It is assumed that at the intermediate steps the level densities decrease moving towards the ridge. This reasonable assumption causes the intermediate level densities to cancel out in the product of successive step probabilities given by Eq. (5.1). For the path down from the ridge to the symmetric valley the probabilities from Eq. (5.1) will be 1 with a similar assumption. If only one such scenario, with the sequence of steps giving the probability $P^{(n)}_{v\to r}$, was responsible for all of the symmetric-fission events, the ratio (5.5) would give the energy dependence. The low-E^* level density in the numerator, $\rho_r(I, E^*(\boldsymbol{\chi}_r))$, shows the pairing structure giving a non-monotonic energy dependence, while the level density in the denominator, $\rho_v(I, E^*(\boldsymbol{\chi}_v))$, is for higher local excitation energies, and thus is a smooth monotonically increasing function only influencing the overall slope of the energy dependence. Although the calculations allow many random-walk paths leading to symmetric shapes, the level densities at points along the ridge likely play a large role in determining the energy dependence.

5.4 Outlook

To limit the computation time, the microscopic level densities are calculated for local excitation energies up to 6 MeV, and then extrapolated using a fitted formula. This extrapolation is motivated by the general properties of level densities and tested to work well for the local excitation energies relevant for the current study. For high excitation energies the level density should converge to that of a Fermi gas with local excitation energy determined only by the macroscopic liquid-drop energy. With the shape-dependent matching constant $C(\boldsymbol{\chi})$ (Eq. (8) of paper V), used to connect to the microscopic level densities, it is not guaranteed that the absolute value of the level density agrees with the limiting case. If the extrapolation recipe can be improved so that it always gives the correct high-energy limit, fission at higher excitation energies can be studied. This would allow the study of multi-chance fission for highly excited compound systems.

Another important fission observable is the kinetic energies of the fragments. The random-walk approach assumes a high dissipation, and thus no collective kinetic energy in the shape evolution up to scission. The final kinetic energies obtained with this assumption can be investigated by considering the fragment kinetic energy implied by the static Coulomb repulsion for the different scission shapes obtained in the calculations.

In the study in paper V the proton-to-mass ratio Z/A of the fragments cannot vary from that of the compound nucleus. The system is modeled as an excited even-even compound system for all shapes, so the odd-even staggering seen in the experimental yields cannot be described. An extension of the random-walk method including a proton-neutron asymmetry degree of freedom was proposed in Ref. [110]. Extending the microscopic level-density approach to model situations leading to odd numbers of quasiparticles in each fragment might be challenging, but if it can be achieved it would offer an interesting study of how the level densities, which are qualitatively different for even-even and odd nuclei, affect the odd-even staggering of the yields.

In general, fission is a very challenging process to describe fully microscopically in terms of interacting nucleons. Several aspects of the assumptions leading to, and implicit in, the random-walk description could be subjects for detailed investigation. The random walk approach is motivated by the strong-dissipation limit of the classical Langevin equations together with the wall-formula for dissipation [23]. The good description of fission yield distributions motivates work on clarifying the microscopic foundations of the approach. It might be illuminating to study the approximations needed to go from a general quantum-mechanical many-body approach to a random-walk on the lattice of shapes. As a starting point one could perhaps consider the states contained in the level density at the different lattice sites as basis states for the time evolution. Framing the problem in this way and working out the needed assumptions might guide work on further improvements.

References

[1] U. Forsberg, *PhD dissertation: Element 115* (Division of Nuclear Physics, Lund University, Lund, 2016).

[2] The ENSDF database: `http://www.nndc.bnl.gov/ensdf/ensdf/ensdf-info.jsp` (2016).

[3] J. Erler, N. Birge, M. Kortelainen, W. Nazarewicz, E. Olsen, A. M. Perhac, and M. Stoitsov, Nature **486**, 509 (2012).

[4] A. Sobiczewski and K. Pomorski, Progress in Particle and Nuclear Physics **58**, 292 (2007).

[5] Kragh, Helge, Eur. Phys. J. H **38**, 411 (2013).

[6] N. Bohr and J. A. Wheeler, Phys. Rev. **56**, 426 (1939).

[7] W. D. Myers and W. J. Swiatecki, Nuclear Physics **81**, 1 (1966).

[8] S. G. Nilsson *et al.*, Nucl. Phys. A **131**, 1 (1969).

[9] Y. Oganessian and V. Utyonkov, Nucl. Phys. A **944**, 62 (2015), special Issue on Superheavy Elements.

[10] L. Öhrström and J. Reedijk, Pure App. Chem. **preprint** (2016), `https://iupac.org/iupac-announces-the-names-of-the-elements-113-115-117-and-118/`.

[11] M. Asai, F. Heßberger, and A. Lopez-Martens, Nucl. Phys. A **944**, 308 (2015), special Issue on Superheavy Elements.

[12] D. Ackermann, Nucl. Phys. A **944**, 376 (2015), special Issue on Superheavy Elements.

[13] G. T. Seaborg and W. D. Loveland, *The elements beyond uranium* (John Wiley & Sons, New York, 1990).

[14] M. Bender, P.-H. Heenen, and P.-G. Reinhard, Rev. Mod. Phys. **75**, 121 (2003).

[15] M. Bender and P.-H. Heenen, Phys. Rev. C **78**, 024309 (2008).

[16] J. L. Egido, Physica Scripta **91**, 073003 (2016).

[17] D. Regnier, N. Dubray, N. Schunck, and M. Verrière, Phys. Rev. C **93**, 054611 (2016).

[18] J. Sadhukhan, W. Nazarewicz, and N. Schunck, Phys. Rev. C **93**, 011304 (2016).

[19] J. Engel, M. Bender, J. Dobaczewski, W. Nazarewicz, and R. Surman, Phys. Rev. C **60**, 014302 (1999).

[20] M. T. Mustonen and J. Engel, Phys. Rev. C **87**, 064302 (2013).

[21] D. Rudolph *et al.*, Phys. Rev. Lett. **111**, 112502 (2013).

[22] J. Randrup and P. Möller, Phys. Rev. Lett. **106**, 132503 (2011).

[23] J. Randrup, P. Möller, and A. J. Sierk, Phys. Rev. C **84**, 034613 (2011).

[24] H. Uhrenholt, S. Åberg, A. Dobrowolski, T. Døssing, T. Ichikawa, and P. Möller, Nucl. Phys. A **913**, 127 (2013).

[25] P. Navrátil, S. Quaglioni, I. Stetcu, and B. R. Barrett, Journal of Physics G: Nuclear and Particle Physics **36**, 083101 (2009).

[26] G. Hagen, T. Papenbrock, D. J. Dean, and M. Hjorth-Jensen, Phys. Rev. C **82**, 034330 (2010).

[27] B. R. Barrett, P. Navrátil, and J. P. Vary, Progress in Particle and Nuclear Physics **69**, 131 (2013).

[28] K. Pomorski and J. Dudek, Phys. Rev. C **67**, 044316 (2003).

[29] P. Möller, A. Sierk, T. Ichikawa, and H. Sagawa, Atomic Data and Nuclear Data Tables **109-110**, 1 (2016).

[30] J. Erler, P. Klüpfel, and P.-G. Reinhard, Journal of Physics G: Nuclear and Particle Physics **38**, 033101 (2011).

[31] S. Fayans, S. Tolokonnikov, E. Trykov, and D. Zawischa, Nucl. Phys. A **676**, 49 (2000).

[32] P. Ring and P. Schuck, *The nuclear many-body problem* (1st ed. Springer-Verlag, New York, 1980).

[33] J. Dobaczewski and W. Nazarewicz, in *Fifty Years of Nuclear BCS: Pairing in Finite Systems* (World Scientific Publishing Co, 2013) pp. 40–60.

[34] A. L. Fetter and J. D. Walecka, *Quantum Theory of Many-Particle Systems* (Dover publications, Mineola, New York, 2003).

[35] I. Stetcu and J. Rotureau, Progress in Particle and Nuclear Physics **69**, 182 (2013).

[36] B. D. Day, Rev. Mod. Phys. **39**, 719 (1967).

[37] H. Köhler, Physics Reports **18**, 217 (1975).

[38] S. Bogner, R. Furnstahl, and A. Schwenk, Progress in Particle and Nuclear Physics **65**, 94 (2010).

[39] K. Hebeler, S. K. Bogner, R. J. Furnstahl, A. Nogga, and A. Schwenk, Phys. Rev. C **83**, 031301 (2011).

[40] S.-H. Shen, J.-N. Hu, H.-Z. Liang, J. Meng, P. Ring, and S.-Q. Zhang, Chinese Physics Letters **33**, 102103 (2016).

[41] T. Skyrme, Nuclear Physics **9**, 615 (1958-1959).

[42] D. Vautherin and D. M. Brink, Phys. Rev. C **5**, 626 (1972).

[43] E. Perlińska, S. G. Rohoziński, J. Dobaczewski, and W. Nazarewicz, Phys. Rev. C **69**, 014316 (2004).

[44] M. Stoitsov, J. Dobaczewski, W. Nazarewicz, and P. Ring, Comp. Phys. Comm. **167**, 43 (2005).

[45] J. C. Slater, Phys. Rev. **81**, 385 (1951).

[46] J. W. Negele and D. Vautherin, Phys. Rev. C **5**, 1472 (1972).

[47] S. Bogner, "Lecure notes, TALENT school: Density functional theory and self-consistent methods (first edition), Trento 2014," `https://wikihost.nscl.msu.edu/TalentDFT/lib/exe/fetch.php?media=dme.pdf`.

[48] B. G. Carlsson, J. Dobaczewski, J. Toivanen, and P. Veselý, Comp. Phys. Comm. **181**, 1641 (2010).

[49] J. Suhonen, *From Nucleons to Nucleus*, Theoretical and Mathematical Physics (Springer-Verlag Berlin Heidelberg, 2007).

[50] Y. Nogami, Phys. Rev. **134**, B313 (1964).

[51] H. J. Lipkin, Annals of Physics **9**, 272 (1960).

[52] T. R. Rodríguez, J. L. Egido, and L. M. Robledo, Phys. Rev. C **72**, 064303 (2005).

[53] Wikimedia commons: `https://commons.wikimedia.org/wiki/File:Alpha_Decay.svg` (2007).

[54] G. Gamow, Zeitschrift für Physik **51**, 204 (1928).

[55] R. G. Lovas, R. J. Liotta, A. Insolia, K. Varga, and D. S. Delion, Phys. Rep. **294**, 265 (1998).

[56] D. S. Delion, *Theory of particle and cluster emission*, Lecture notes in physics No. 819 (Springer, 2010).

[57] P. Descouvemont and D. Baye, Rep. Prog. Phys. **73**, 036301 (2010).

[58] R. G. Thomas, Progress of Theoretical Physics **12**, 253 (1954).

[59] A. Bohm, M. Gadella, and G. B. Mainland, Am. J. Phys. **57**, 1103 (1989).

[60] A. T. Kruppa and W. Nazarewicz, Phys. Rev. C **69**, 054311 (2004).

[61] H.-D. Zeh, Z. Phys. **175**, 490 (1963).

[62] H. J. Mang, Annual Review of Nuclear Science **14**, 1 (1964).

[63] R. de la Madrid and M. Gadella, American Journal of Physics **70** (2002).

[64] M. Abramowitz and I. Stegun, *Handbook of Mathematical Functions*, Applied mathematics series (National Bureau of Standards, 1972).

[65] N. Michel, Comp. Phys. Comm. **176**, 232 (2007).

[66] I. Tonozuka and A. Arima, Nucl. Phys. **A323**, 45 (1979).

[67] G. P. Kamuntavičius, R. K. Kalinauskas, B. R. Barret, S. Mickevičius, and D. Germanas, Nucl. Phys. A **695**, 191 (2001).

[68] T. Fliessbach, Z. Phys. A **272**, 39 (1975).

[69] E. Chabanat, P. Bonche, P. Haensel, J. Meyer, and R. Schaeffer, Nucl. Phys. A **635**, 231 (1998).

[70] T. Fliessbach and H. Mang, Nucl. Phys. **A263**, 75 (1976).

[71] R. I. Betan and W. Nazarewicz, Phys. Rev. C **86**, 034338 (2012).

[72] K. Varga, R. Lovas, and R. Liotta, Nucl. Phys. A **550**, 421 (1992).

[73] B. G. Carlsson, D. E. Ward, and S. Åberg, EPJ Web of Conferences **131**, 08002 (2016).

[74] M. V. Stoitsov, N. Schunck, M. Kortelainen, N. Michel, H. Nam, E. Olsen, J. Sarich, and S. Wild, Comp. Phys. Comm. **184**, 1592 (2013).

[75] The ENSDF database: `http://www.nndc.bnl.gov/ensdf/` (2016).

[76] P. Jachimowicz, M. Kowal, and J. Skalski, Phys. Rev. C **89**, 024304 (2014).

[77] I. Brida, S. C. Pieper, and R. B. Wiringa, Phys. Rev. C **84**, 024319 (2011).

[78] Y. Shi, J. Dobaczewski, and P. T. Greenlees, Phys. Rev. C **89**, 034309 (2014).

[79] M. Kortelainen, J. McDonnell, W. Nazarewicz, P.-G. Reinhard, J. Sarich, N. Schunck, M. V. Stoitsov, and S. M. Wild, Phys. Rev. C **85**, 024304 (2012).

[80] P. Rozmej, K. Boning, and A. Sobiczewski, *Proceedings of the XXIV International Winter Meeting on Nuclear Physics, Bormio, Italy*, edited by I. Iori (Ric. Sci. Educ. Permanente, Milano, 1986) p. 567.

[81] I. Ragnarsson and P. B. Semmes, Hyperfine Interactions **43**, 423 (1988).

[82] C. F. v. Weizsäcker, Zeitschrift für Physik **96**, 431 (1935).

[83] V. Strutinsky, Nucl. Phys. A **95**, 420 (1967).

[84] V. Strutinsky, Nucl. Phys. A **122**, 1 (1968).

[85] W. Nazarewicz, M. Riley, and J. Garrett, Nucl. Phys. A **512**, 61 (1990).

[86] M. Bolsterli, E. O. Fiset, J. R. Nix, and J. L. Norton, Phys. Rev. C **5**, 1050 (1972).

[87] B. G. Carlsson, *PhD dissertation: Models for rotating nuclei : cranking and rotor+particles coupling* (Division of Mathematical Physics, LTH, Lund University, Lund, 2007).

[88] I. Ragnarsson and S. G. Nilsson, *Shapes and Shells in Nuclear Structure* (Cambidge University Press, 1995).

[89] J. Rekstad, T. Engeland, and E. Osnes, Nucl. Phys. A **330**, 367 (1979).

[90] B. G. Carlsson and I. Ragnarsson, Phys. Rev. C **74**, 011302 (2006).

[91] J. Boisson, R. Piepenbring, and W. Ogle, Physics Reports **26**, 99 (1976).

[92] A. Covello, A. Gargano, and N. Itaco, Phys. Rev. C **56**, 3092 (1997).

[93] A. Covello, A. Gargano, and N. Itaco, Phys. Rev. C **65**, 044320 (2002).

[94] C. J. Gallagher and S. A. Moszkowski, Phys. Rev. **111**, 1282 (1958).

[95] H. J. Krappe and K. Pomorski, *Theory of Nuclear Fission*, Lecture notes in physics No. 838 (Springer, 2012).

[96] A. Bulgac, P. Magierski, K. J. Roche, and I. Stetcu, Phys. Rev. Lett. **116**, 122504 (2016).

[97] K. Mazurek, C. Schmitt, and P. N. Nadtochy, Phys. Rev. C **91**, 041603 (2015).

[98] P. Möller and J. R. Nix, Nucl. Phys. A **361**, 117 (1981).

[99] P. Möller, J. R. Nix, W. D. Myers, and W. J. Swiatecki, At. Data Nucl. Data Tables **59**, 185 (1995).

[100] P. Möller, B. Pfeiffer, and K.-L. Kratz, Phys. Rev. C **67**, 055802 (2003).

[101] P. Möller, A. J. Sierk, T. Ichikawa, A. Iwamoto, R. Bengtsson, H. Uhrenholt, and S. Åberg, Phys. Rev. C **79**, 064304 (2009).

[102] P. Möller, D. G. Madland, A. J. Sierk, and A. Iwamoto, Nature **409**, 785 (2001).

[103] J. Randrup and P. Möller, Phys. Rev. C **88**, 064606 (2013).

[104] P. Möller and J. Randrup, Phys. Rev. C **91**, 044316 (2015).

[105] A. Bohr and B. R. Mottelson, *Nuclear Structure Volume II: Nuclear Deformations* (World Scientific, Singapore, 1998).

[106] G. Leander and R. Sheline, Nucl. Phys. A **413**, 375 (1984).

[107] S. Åberg, B. Carlsson, T. Døssing, and P. Möller, Nucl. Phys. A **941**, 97 (2015).

[108] B. M. S. Bjørnholm and A. Bohr, *Physics and Chemistry of Fission, Proceedings of a Conference at Rochester*, Vol. 1 (IAEA, Vienna, 1974) p. 367.

[109] R. V. Jolos, N. Minkov, and W. Scheid, Phys. Rev. C **72**, 064312 (2005).

[110] P. Möller and T. Ichikawa, Eur. Phys. J. A **51**, 173 (2015).

Appendix A

Computer codes developed

To perform the calculation of formation amplitudes in papers I-III, and the random-walk calculations in paper V, two computer codes, FAH and FM, were developed. This appendix contains a brief description of these codes and how to run the calculations. Both codes are written in Fortran 2003, and employ the Fortran namelist construction for input.

A.1 α-decay codes

An α-decay calculation involves three codes: HOSPHE, to perform the SHFB calculations, the code FAH for the formation amplitudes, and a Coulomb-penetrability code FGAMC. The codes produce output files used as input in the successive calculations, as illustrated below,

$$\text{HOSPHE} \times 2 \rightarrow \text{FAH} \rightarrow \text{FGAMC}.$$

In the first step, HOSPHE is run twice, once for the mother and once for the daughter nucleus. In these calculations, the HFB U and V matrices and the quasiparticle energies E_k are saved to the files `filename_m.hfbn`, and `filename_m.hfbp`, where `filename_m` is the input given for the "`file`" namelist variable of HOSPHE for the mother nucleus calculation. Another filename must be used for the daughter nucleus calculation. Both calculations must be performed using the same oscillator frequency and the same truncation of the spherical oscillator basis.

These files are then read by FAH. This code computes the formation amplitudes and prints them to a file that can be read by FGAMC to obtain the decay width $\Gamma(r_V)$, Eq. (3.35).

A.1.1 Formation-amplitude code

The code FAH, where the name stands for "Formation Amplitude Hosphe", calculates the formation amplitudes. Equation (3.51) expressed in the spherical oscillator basis is used, with the four-particle transfer amplitude factorized into a proton and a neutron two-particle transfer amplitude as described in Sec. 3.2.2. The calculations are controlled via the Fortran namelist `&inDataFaH`. An example run-script for Linux is given below:

```
#!/bin/bash

fah << end
&inDataFaH oddDecay = 2,
qp_l_M = 3, qp_j2_M = 5, qp_nr_M = 1,
qp_l_D = 1, qp_j2_D = 3, qp_nr_D = 1,
nmax = 30, bN = 2.22576754, step = 0.125, dimr = 200,
outfileFa = 'fah.z84n119.SLy4.MixP.Nmax30',
fileHFBmatMn = 'z84n119.SLy4.MixP.Nmax30.hfbn',
fileHFBmatMp = 'z84n119.SLy4.MixP.Nmax30.hfbp',
fileHFBmatDn = 'z82n117.SLy4.MixP.Nmax30.hfbn',
fileHFBmatDp = 'z82n117.SLy4.MixP.Nmax30.hfbp'/
end
```

This calculation is for the ground-state-to-ground-state α-decay of ${}^{203}_{84}\mathrm{Po}_{119}$, where the mother-nucleus ground state (gs) is described by a $f_{5/2}$ one-quasiparticle (qp) state, and the gs of the daughter nucleus ${}^{199}_{82}\mathrm{Pb}_{117}$ is described by a $p_{3/2}$ one-qp state. The namelist entries needed for a calculation, and the values used in this example are listed below:

- `oddDecay = 2`: Flag to control if even-even ground states or one-qp states in odd-A nuclei are considered, even-even (0), odd-Z-even-N (1), even-Z-odd-N (2).
- `qp_l_M = 3`: Orbital angular-momentum quantum number l for the quasiparticle in the mother nucleus.
- `qp_j2_M = 5`: Total angular-momentum quantum number $2j$ for the quasiparticle in the mother nucleus.
- `qp_nr_M = 1`: Order in quasiparticle energy E_k among quasiparticle states with the same lj.
- The same namelist entries as the three above with `M` replaced by `D` refer to the quasiparticle in the daughter nucleus. If `oddDecay = 0`, these six quasiparticle indexes are not used.

- `nmax = 30`: Largest major oscillator shell $N_{\max}$ used to expand the HFB wave function.
- `bN = 2.22576754`: Oscillator length $b = \sqrt{\frac{\hbar}{m\omega}}$ in fm used in the spherical oscillator basis. Here m is the nucleon mass and ω is the oscillator frequency.
- `step = 0.125`: Distance between radial points Δr in fm.
- `dimr = 200`: Number of radial points where the formation amplitudes $f_{kl_k}(r)$ are evaluated, $r = n\Delta r, \quad n = 1, 2, \ldots,$ `dimr`.
- `outfileFa = 'fah.z84n119.SLy4.MixP.Nmax30'`: Base for filenames of the output files generated by the code. These files will start with the base followed by different suffixes.
- `fileHFBmatMn = 'z84n119.SLy4.MixP.Nmax30.hfbn'`: Name of the file containing the U and V matrix elements for the neutron part of the mother nucleus HFB vacuum. As shown in the example script the three other required input files are specified in a similar way.

A.1.2 Coulomb-penetrability code

To compute the Coulomb penetrabilities, Eq. (3.38), and the decay widths, Eq. (3.36), the code FGAMC is used. It is written in C++ and acts as a wrapper around N. Michels Coulomb wave-function code [65]. An example run-script for the same α-decay scenario considered in the previous section is given below:

```
#!/bin/bash

oddD=2;
LM=3; J2M=5; nrM=1;
LD=1; J2D=3; nrD=1;
dimr=200;
ND=117; ZD=82;
Qa=5.496;
rtscaling=1.0;

if [ $oddD == 0 ]
then

fgamc << end
```

```
fah.z84n119.SLy4.MixP.Nmax30
G.z84n119.SLy4.MixP.Nmax30
$oddD
$dimr
$ND
$ZD
$Qa
$rtscaling
end

else

fgamc << end
fah.z84n119.SLy4.MixP.Nmax30
G.z84n119.SLy4.MixP.Nmax30
$oddD
$LM
$J2M
$nrM
$LD
$J2D
$nrD
$dimr
$ND
$ZD
$Qa
$rtscaling
end

fi
```

In this bash script the different numerical values are stored in the local variables `oddD`, `LM`, `J2M`, `nrM`, `LD`, `J2D`, `nrD`, `dimr`, `ND`, `ZD`, `Qa`, and `rtscaling`. These act as placeholders and generate a text file which is read line-by-line by the code FGAMC. The first two lines of the file is the base filename for the results from FAH, here chosen to be "`fah.z84n119.SLy4.MixP.Nmax30`", and a base filename for the output generated by FGAMC, "`G.z84n119.SLy4.MixP.Nmax30`". Most of the values to be put in the different lines of the input to the Coulomb-penetrability code should be obvious by comparing with the previous section. There are four additional numbers in the input: The number of neutrons `ND` and protons `ZD` of the daughter nucleus. The Q-value for the decay `Qa`. The last additional input controls how the touching radius r_t is calculated. For `rtscaling=1.0`,

Eq. (3.53) is used, otherwise a different touching radius is used,

$$r_t \rightarrow \texttt{rtscaling} \times r_t.$$

Note that the number of lines to be read by the code depends on the value of `oddD`.

A.2 Fission random-walk code

The random-walk calculation for the fission yields is performed with the code FM, where the name is short for "Fission Metropolis". The code reads files containing the potential energy and the level densities at the different lattice points. This data is stored in memory and used to compute the probabilities to accept proposed steps during the random walk. The necessary interpolation and extrapolation of the level density is performed by the code during the random walk.

The input to specify parameters for the run and the names of the various input data files are supplied via the Fortran namelist `&inDataFM`. Some of the namelist variables and example values are listed below:

- `outfile='z92.n142.Etot10.048.spin3.iter1e5sm2e5.rc2.5'`: Base for the names of various output files generated by the program. The different files start with this base and end with different suffixes.
- `Z=92, N=142`: Number of protons Z and neutrons N of the compound nucleus.
- `Enertot = 10.048`: Total energy E of the system, measured relative to the macroscopic energy for a spherical shape.
- `rneck_c = 2.5`: Critical neck radius c_0 where the random walk is ended and the mass asymmetry is binned.
- `start_I = 11, start_J = 1, start_K = 13, start_L = 13, start_M = 2`: Starting point for the random walks in terms of the lattice indexes I, J, K, L, M.
- `iter_max = 100000`: Number of random walks performed to obtain the yield.
- `steps_max = 200000`: Cutoff on the number of steps in a given random walk, discussed in Sec. IIIA of paper V.
- `ap_model = 3`: Allows to use different formulas to determine the probability to accept a proposed step in the random walk: `1` – the recipe employed in Ref. [22] is used, `3` – the microscopic level densities are used as in paper V, `9` – the method employed in Ref. [103] is used.

- `use_wall_bias = .true., wall_bias_II = 8`: Controls if the "wall" bias should be used, and the elongation index of the "wall".

- `level_density_extrapol_ver = 3`: Controls the method used to extrapolate the microscopic level density to higher energies. When equal to 3, the method of paper V is used.

- `fg_e0param = 10.482643, Edamping = 13.178511, EdampingPair = 4.067328`: The parameters e_0, $E_{\mathrm{d,sh}}$, and $E_{\mathrm{d,pc}}$ defined in Sec. II of paper V.

- `filename_pot5D = 'pot5D092234.dat'`: Name of the file containing the potential energy at the different lattice sites.

- `filename_emac5D = 'emacr092234.dat'`: Name of the file containing the macroscopic energy at the different lattice sites.

- `filename_rneck = 'neck5D.dat'`: Name of the file containing the neck radius for each shape.

- `filename_unphys = 'unphysical_points_3QS.dat'`: Name of a file containing the lattice locations of unphysical shapes for which level density calculations are not performed.

- `is_read_levsum = .true., filename_levsum = 'levsum092234.dat'`: Instructs the code to read level densities from the specified file. If the level densities are not used, i.e. if a different formula to accept a step that does not require the microscopic level density is used, these two keywords can be omitted from the input. Different formats of the level density file can be accepted by the code trough the use of various flags documented in the start of the source code to the main program.

- `spin_select_levsum = 3`: Selects the total angular momentum I for the compound nucleus. The level density for the chosen I-value is used in the calculation of the probability to accept a step in the random walk.

- `is_combine_par_levsum = .true.`: If the keyword `.true.` is used, the sum of the level density for positive and negative parity states are used to determine the random walk step probabilites. If `.false.` only one of the parities is used.

- `par_select_levsum = 1`: Controls which parity is used if `is_combine_par_levsum = .false.`, `1` is positive parity, `-1` is negative parity.